Synthesis of Ferrites as an Electrode Material for Supercapacitor Application

By

Hina Maqsood

(Registration No: 00000327641)

School of Chemical and Materials Engineering

National University of Sciences and Technology (NUST)

Islamabad, Pakistan

(2024)

Synthesis of Ferrites as an Electrode Material for Super capacitor Application

By

Name: Hina Maqsood

Registration. No: 00000327641

A thesis submitted to the National University of Sciences and Technology, Islamabad,

in partial fulfillment of the requirements for the degree of

Master of Science in

Material and Surface Engineering

Supervisor: Dr. Iftikhar Hussain Gul

School of Chemical and Materials Engineering

National University of Sciences & Technology (NUST)
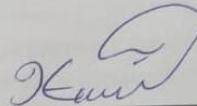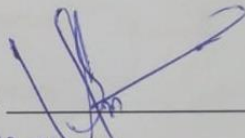
Islamabad, Pakistan

(2024)

THESIS ACCEPTANCE CERTIFICATE

Certified that final copy of MS Thesis entitled "Synthesis of Ferrites as an Electrode Material for Supercapacitor Application" written by Ms **Hina Maqsood** (Registration No 00000327641), of School of Chemical & Materials Engineering (SCME) has been vetted by undersigned, found complete in all respects as per NUST Statues/Regulations, is free of plagiarism, errors, and mistakes and is accepted as partial fulfillment for award of MS degree. It is further certified that necessary amendments as pointed out by GEC members of the scholar have also been incorporated in the said thesis.
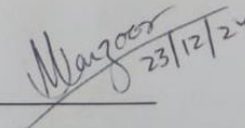
Signature: _____

Name of Supervisor: **Dr Iftikhar Hussian Gul**

Date: ___17/12/2024___

Signature (HOD): _____

Date: ___20-12-24___

Signature (Dean/Principal): _____

Date:_____

TH-1 FORM

National University of Sciences & Technology (NUST)

MASTER'S THESIS WORK

Formulation of Guidance and Examination Committee (GEC)

Name: Hina Maqsood   NUST Reg No:00000327641

Department: Department of Materials Engineering   Specialization:Master of Science in Materials & Surface Engineering

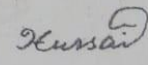Credit Hour Completed: 24.0   CGPA: 3.0

Course Work Completed

S/No:	Code:	Title:	Core/Elective:	CH:	Grade:
1.	MSE-821	Mechanical Behaviour Of Materials	Compulsory	3.0	C+
2.	RM-898	Research Methodology	Additional	2.0	Q
3.	MSE-811	Materials Thermodynamics	Compulsory	3.0	C+
4.	MSE-812	Phase Transformation & Microstructures	Compulsory	3.0	F
5.	MSE-851	Surface Engineering & Characterisation *	Compulsory	3.0	C+
6.	MSE-854	Characterization Of Materials	Elective	3.0	B
7.	NSE-813	Essentials of Nanoscience and Engineering	Elective	3.0	B+
8.	MSE-881	Manufacturing Processes	Elective	3.0	B+
9.	MSE-821	Mechanical Behaviour Of Materials	Improve	3.0	B
10.	MSE-952	Materials For Biomedical Applications	Elective	3.0	B
11.	MSE-812	Phase Transformation & Microstructures	Repeat	3.0	C
12.	MSE-851	Surface Engineering & Characterisation	Improve	3.0	B+
13.	MSE-811	Materials Thermodynamics	Improve	3.0	W

Date 29 - May - 2023
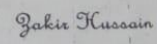
Student's Signature

Thesis Committee

Name: Iftikhar Hussain Gul (Supervisor)
Department: Department of Materials Engineering

Signature _Hussain_

Name: Sofia Javed (Internal)
Department: Department of Materials Engineering

Signature

Name: Zakir Hussain (Internal)
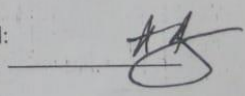Department: Department of Materials Engineering

Signature _Zakir Hussain_

Date: 29 - May - 2023

Signature of Head of Department:

APPROVAL

Date: 29 - May - 2023

Signature of Dean/Principal:

School of Chemical & Materials Engineering (SCME) (SCME) H-12 Campus,

TH-4 FORM

National University of Sciences &Technology (NUST)

FORM TH-4

MASTER'S THESIS WORK

We hereby recommend that the dissertation prepared under our supervision by
Regn No & Name: **00000327641 Hina Maqsood** .

Title: **Synthesis of Ferrites as an Electrode Material for Supercapacitor Application.**

Presented on: **26 Sep 2024**   at: **1500 hrs in SCME (on MS Teams)**

Be accepted in partial fulfillment of the requirements for the award of Masters of Science degree in **Materials & Surface Engineering.**

Guidance & Examination Committee Members

Name: **Dr Sofia Javed**   Signature: _____

Name: **Dr Zakir Hussain**   Signature: _____

Supervisor's Name: **Dr Iftikhar Hussain Gul**   Signature: _____

Dated: 26/9/2024

Head of Department   **Dean/Principal**

Date 10/10/24   Date 10/10/24

School of Chemical &Materials Engineering (SCME)

AUTHOR'S DECLARATION

I <u>Hina Maqsood</u> hereby state that my MS thesis titled <u>"Synthesis of Ferrites as an electrode material for Supercapacitor application"</u> is my own work and has not been submitted previously by me for taking any degree from National University of Sciences and Technology, Islamabad or anywhere else in the country/ world.

At any time if my statement is found to be incorrect even after I graduate, the university has the right to withdraw my MS degree.

Name of Student: <u>Hina Maqsood</u>

Date: <u>22/ 08/ 2024</u>

PLAGIARISM UNDERTAKING

I solemnly declare that research work presented in the thesis titled "Synthesis of Ferrites as an Electrode Material for Supercapacitor Application" is solely my research work with no significant contribution from any other person. Small contribution/ help wherever taken has been duly acknowledged and that complete thesis has been written by me.

I understand the zero-tolerance policy of the HEC and National University of Sciences and Technology (NUST), Islamabad towards plagiarism. Therefore, I as an author of the above titled thesis declare that no portion of my thesis has been plagiarized and any material used as reference is properly referred/cited.

I undertake that if I am found guilty of any formal plagiarism in the above titled thesis even after award of MS degree, the University reserves the rights to withdraw/revoke my MS degree and that HEC and NUST, Islamabad has the right to publish my name on the HEC/University website on which names of students are placed who submitted plagiarized thesis.

Student Signature:

Name: Hina Maqsood

DEDICATION

I dedicate this thesis to my dearest **parents**, **husband**, and **brothers**, with the deepest love and thanks. Throughout this journey, your unfailing support, encouragement, and sacrifices have been my lighthouse. This achievement is a testament to the strength you have given me

ACKNOWLEDGMENTS

I am incredibly grateful to Allah Almighty the most merciful and the most gracious, the source of all strength and wisdom, for giving me the perseverance to finish my thesis and for leading me through the difficult knowledge-gathering process. His boundless blessings have brightened my way and deepened my comprehension, enabling me to overcome obstacles and reach this important milestone.

I would like to express my sincere gratitude to my wonderful supervisor, Dr. Iftikhar Hussain Gul, whose constant support, constructive criticism, and unflinching guidance have greatly influenced the direction this study has taken.

I owe Muhammad Zafar, Anum Rabab, and Varda Shakeel for their unwavering support and encouragement throughout this academic endeavor. The atmosphere of friendship and intellectual advancement fostered by your conversations, exchanges of experiences, and mutual support has added to the satisfaction of this journey.

I also want to express my thanks to my dear husband whose faith in my abilities, constant love, and sacrifices have been the foundation of my success. My gratitude also extends to my parents and brothers, your unwavering support, tolerance, and sacrifices have helped me become the person I am today, and for that, I will always be grateful.

In conclusion, I am humbled by the kindness and generosity I have encountered along the path, and my thesis serves as a monument of the combined efforts and contributions of many people. I extend my heartfelt gratitude to everyone who has contributed, in any way, to my academic endeavors. May Allah reward each one of us in our endeavors, and may this work make a constructive contribution to the field of knowledge.

With Profound Gratitude,

Hina Maqsood

TABLE OF CONTENT

LIST OF FIGURES

LIST OF TABLES

ABSTRACT

Ferrites have been widely investigated for supercapacitor application. The doping of ferrites with various metal enhances the electrochemical performance. In this study ferrite-based electrodes were synthesized using coprecipitation method. The synthesized materials are $ZnFe_2O_4$, $Zn_{0.5}Mg_{0.5}Fe_2O_4$, $Zn_{0.5}Co_{0.5}Fe_2O_4$, and $Zn_{0.5}Mg_{0.25}Co_{0.25}Fe_2O_4$. X-ray Diffraction confirmed FCC cubic structure of ferrites with the crystallite size of 15,17,10 and 18 nm for $ZnFe_2O_4$, $Zn_{0.5}Mg_{0.5}Fe_2O_4$, $Zn_{0.5}Co_{0.5}Fe_2O_4$, and $Zn_{0.5}Mg_{0.25}Co_{0.25}Fe_2O_4$ respectively. Scanning electron microscopy revealed that the particles are spherical and the average size is 55 nm, 68.1 nm, 33.1 nm and 143 nm respectively. Elemental composition was determined by Energy Dispersive X-Ray Spectroscopy. Functional group analysis was done using Fourier Transform Infrared spectroscopy. Synthesized electrode material was then deposited on Ni foam using Nafion as a binder to study their electrochemical properties. The substrates were dried overnight at 60°C in vacuum oven; and the loaded mass on Ni foam was around 0.006-0.008 mg. Electrochemical properties such as specific capacitance, resistance, current density, and discharge time were studied via Cyclic voltammetry (CV), Electrochemical impedance spectroscopy (EIS) and Galvanostatic Charge discharge (GCD). At various scan rates (5 mV/s, 10 mV/s, 20 mV/s, 50 mV/s, 100 mV/s and 200 mV/s), cyclic voltammetry was investigated. Comparative analysis of CV at 5 mVs^{-1} shows the specific capacitance for $Zn_{0.5}Co_{0.5}Fe_2O_4$ as 325.67 F/g. The specific capacitance shown by $ZnFe_2O_4$ is 306.58 F/g, $Zn_{0.5}Mg_{0.5}Fe_2O_4$ is 201.05 F/g and $Zn_{0.5}Mg_{0.25}Co_{0.25}Fe_2O_4$ is 94.527F/g. The Redox peak current increases with increasing scan rates. The shape of the CV represents pseudocapacitive behavior of synthesized electrode. The lowest resistance of 1.15 ohm was exhibited by $Zn_{0.5}Co_{0.5}Fe_2O_4$ followed by $ZnFe_2O_4$(1.6 ohm), $Zn_{0.5}Mg_{0.5}Fe_2O_4$(1.15 ohm) and $Zn_{0.5}Mg_{0.25}Co_{0.25}Fe_2O_4$(1.59 ohm). GCD was done at the current density of 0.5A/g. The capacitance shown by GCD for $ZnFe_2O_4$ is 380.13 F/g, $Zn_{0.5}Mg_{0.5}Fe_2O_4$ is 309.57 F/g, $Zn_{0.5}Co_{0.5}Fe_2O_4$ is 530 F/g and $Zn_{0.5}Mg_{0.25}Co_{0.25}Fe_2O_4$ is 260.96 F/g. Putting together this study lays the foundation for more investigation using $Zn_{0.5}Co_{0.5}Fe_2O_4$ ferrite for supercapacitor application.

CHAPTER 1: INTRODUCTION

1.1 Introduction to Supercapacitors

With the Tremendous increase in energy needs, the development of efficient and clean systems for storage has drawn attention from researchers and developers worldwide. Among many technologies for energy storage, fuel cells, batteries , and supercapacitors which use electrochemical reactions are the most important due to the rise in the need for energy storage worldwide. Compared to traditional capacitors, supercapacitors have many advantages involving quick charging , long life cycles , reduced area densities, and strong resistance to temperature changes, they find extensive use in hybrid cars, microelectronics, airplanes, and smart grids [4, 5]. Nevertheless, this technology still has several issues, such as low energy density and expensive production [5, 6].

In the middle of the 20th century, scientists created electric double-layer capacitors (EDLCs), which had the capacity to store incredibly high charges. Due to the fact that charges build up at the electrode electrolyte interfaces within the electric double layer , these capacitors were subsequently referred to as supercapacitors. Two other versions were developed with the quick development of nanotechnology: asymmetric supercapacitors and pseudo capacitors (PCs). Dielectric materials, which act as separators (Figure: 1.1) between two conductive plates (electrodes), are typically found in capacitors. Examples of these materials include glass, plastic, ceramic, and paper. By applying electrical potential, a potential difference can be created between these plates. As a result, it induces the same electrical field of opposite charges in the dielectric medium. The formula determines the capacitance, or the capacitor's ability to hold charge, and it is evaluated in Farad is as:

$$C = A * \frac{\varepsilon}{d}$$

"C" is the capacitance, "A" is the area of the electrode, "ε" is the permittivity and "d" is the distance between electrodes.
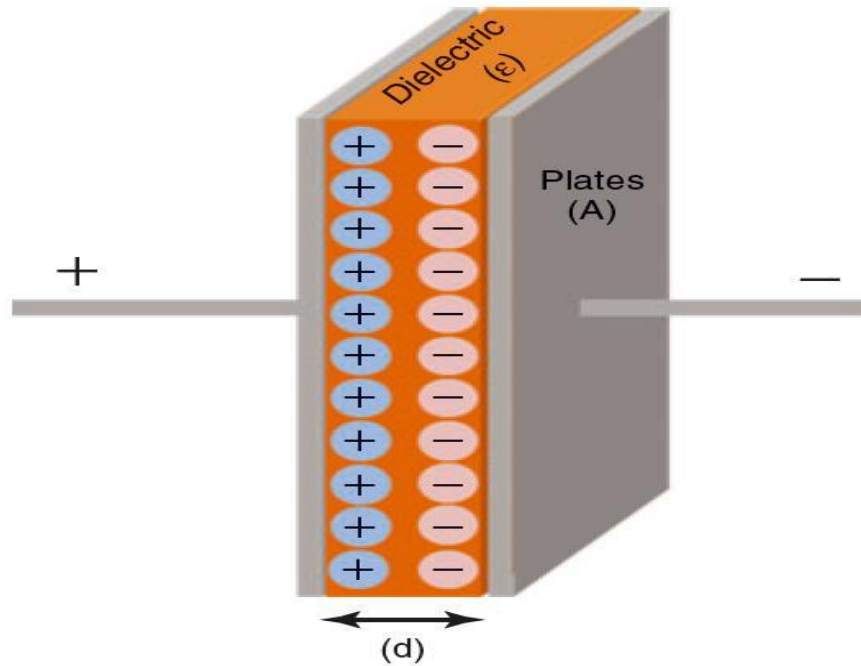
Figure 0.1: Charge Distribution in Dielectric Material in Capacitors [2].

Traditional capacitors and EDLCs share a similar underlying mechanism. Nevertheless, EDLCs store energy between the electrode and electrolyte interface rather than in a dielectric layer. Electrolyte ions enter the active material's micropores when a potential difference is provided between the electrodes of an EDLC. The double-layer thickness at the electrode/electrolyte interface determines the capacitance of EDLCs, as opposed to typical capacitors, where capacitance is based on the separator thickness. Since the thickness of the double layer is significantly less than that of the separator, EDLCs ought to have a larger capacitance than typical capacitors. Moreover, compared to conventional capacitors, the capacitance of EDLCs can be raised by expanding the electrode/electrolyte boundary region. The enhanced wettability of the electrolyte improves ion accessibility into the active material's pores, further increasing the electrochemical characteristics of EDLCs [7]. By combining redox materials pseudocapacitors that perform oxidation-reduction reactions with carbon materials like activated carbon (AC), supercapacitor's

capacitance can be greatly increased. This combination together with the physical interactions of electric double-layer capacitors (EDLCs) at the interface allows for fast and reversible redox reactions. As a result, when

compared to pure carbon-based EDLCs, the capacitive values can increase by ten to one hundred times [8, 9].
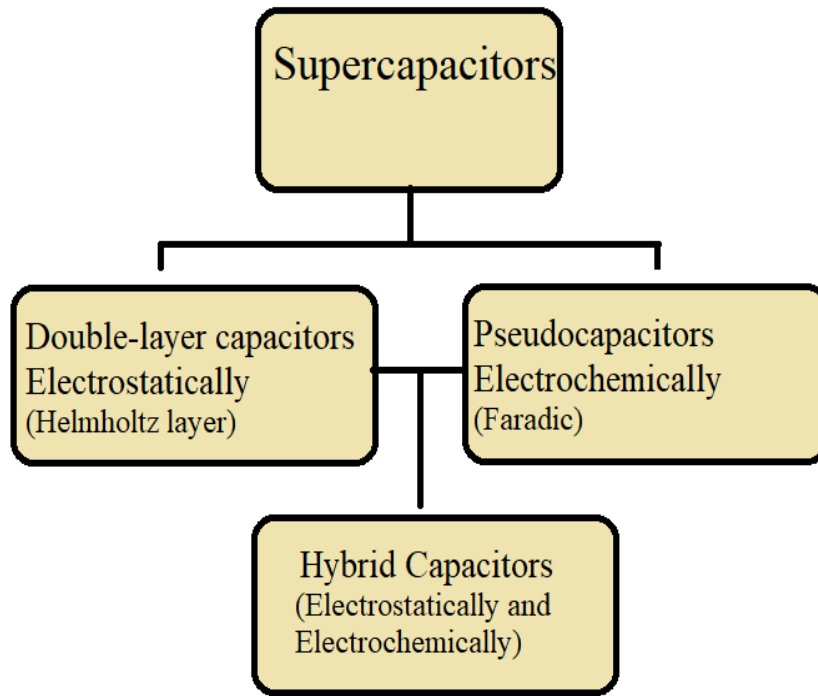
Figure 0.2: Supercapacitor and its Type.

Because of the restrictions of surface area, the charge storage capacity of Electric Double-Layer Capacitors (EDLCs) is largely dependent on the huge surface area of the active material. This results in a poor energy density. However, because they can store more charges through quick surface oxidation and reduction events, pseudo capacitors present a viable substitute. However, low electrical conductivity and unstable structural properties are common problems with pseudocapacitive materials such as polymers and oxides.

"Intercalation-type" electrodes have been created to increase energy density. These substances go through redox processes that are comparable to those in lithium-ion batteries , where the bulk substance is used in processes for energy storage. Despite this, the reactions typically don't undergo a phase transition, which makes them akin to capacitive reactions. The fact that a huge surface area is not required to obtain higher capacity is a significant benefit of intercalation-type materials over EDLCs or pseudocapacitive electrodes. To optimize the pseudo capacity of intercalation materials, it is essential to increase the "oxygen defect sites" and the diffusion rates of oxygen anions within the oxide lattices. Using binder-free electrode materials is one way to achieve this. Conventional electrodes use binders, like polyvinylidene fluoride ,. polytetrafluoroethylene , and Nafion , to attach the active material to the current collector. These binders are inactive and nonconductive , which can interfere with the interconnection of electrode material particles, obstruct ion diffusion channels, and reduce electrical conductance, which consequently leads to a decrease in energy density and cyclic stability.

1.2 Importance of Electrochemical Capacitors

Electrochemical capacitors (ECs) have gained a lot of attention from both the academic and business communities because they greatly outweigh the drawbacks of other available commercial energy storage technologies. ECs have a high energy output density greater than that of batteries and fuel cells, as well as an energy density greater than that of traditional capacitors. Clearly, ECs technology can reduce the energy and power density difference between capacitors and batteries [10-12]. Additionally, because (ECs) undergo far fewer chemical phase transitions during continuous charge and discharge than batteries do, (ECs) have a longer lifespan than batteries. Electrochemical Capacitors are more appealing and adaptable as high-power storage devices because of these important features. The primary energy storage technologies of the future, according to the US Department of Energy (DOE), are ECs and batteries.

ECs might be referred to as "supercapacitors," "ultracapacitors," or "power capacitors" based on the active electrode material or charging method employed. Originally coined by

the Nippon Electric Company (NEC), the name "supercapacitors" which was the first to commercially sell the product as a SuperCapacitor^{TM} made of carbon material, while the U.S. military referred to ECs made of RuO_2 and Ta_2O_5 as "ultracapacitors" [13].

1.3 Difference Between Batteries and Supercapacitors

Electric double-layer capacitors (EDLCs). and pseudocapacitors are examples of supercapacitors. EDLCs rely on surface-controlled charge carrier adsorption and desorption between the electrode and electrolyte interface that doesn't require a faradic reaction. The fast non-faradic reaction leads to a quick charging time and high-power density, while surface-controlled faradic redox reactions between the electrode and electrolyte are the basis for pseudocapacitors. The reaction kinetics are similar to the EDLCs since the reaction takes place near the surface. Consequently, the way that pseudocapacitors and EDLCs. vary is that the former experience faradic reactions while the latter do not [14, 15]. The fact that pseudocapacitors have extremely fast reaction rates and are not diffusion-limited sets them apart from batteries, which have slowed, semi-infinite diffusion of ions in the bulk electrode materials, which limits the kinetics of faradic and redox reactions. In batteries, phase transition usually happens during the charge - discharge process. Battery performance is low due to diffusion-limited redox reaction, resulting in high energy density as shown in Figure 3. Moreover, the charge storage mechanism in pseudocapacitors will be referred to as redox pseudocapacitance if the redox reaction only happened at the active material's surface, where charge carriers are adsorbed on the surface or near to the surface, creating tiny diffusion pathways and

Electric double-layer capacitors (EDLCs) and pseudocapacitors are examples of supercapacitors. EDLCs rely on surface-controlled charge carrier adsorption and desorption between the electrode and electrolyte interface that doesn't require a faradic reaction. The fast non-faradic reaction leads to a quick charging time and high-power density, while surface-controlled faradic redox reactions between the electrode and electrolyte are the basis for pseudocapacitors. The reaction kinetics are similar to the EDLCs since the reaction takes place near the surface. Consequently, the way that pseudocapacitors and EDLCs vary is that the former experience faradic reactions while

the latter do not [14, 15]. The fact that pseudocapacitors have extremely fast reaction rates and are not diffusion-limited sets them apart from batteries, which have slow, semi-infinite diffusion of ions in the bulk electrode materials, which limits the kinetics of faradic and redox reactions.

In batteries, phase transition usually happens during the charge - discharge process. Battery performance is low due to diffusion-limited redox quick charge transfer. The charge storage process will be referred to as intercalation pseudocapacitance if the redox reaction took place in the bulk of the materials, where rapid diffusion of charge carriers in the active material layers happens without any phase transition or structural change. Hence these materials exhibit distinct electrochemical behavior. Difference between elementary features of batteries , capacitors and supercapacitors are shown in Table: 1.1.
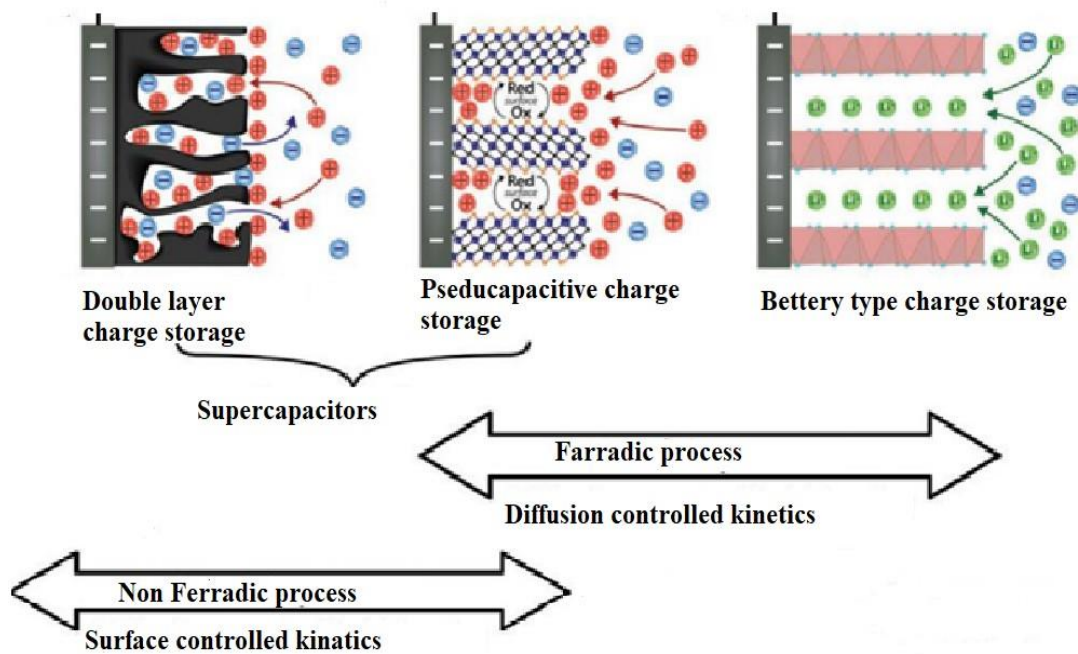
Figure 0.3: Difference Between Battery and Supercapacitors

Table 0.1: Difference between Elementary features of Batteries, Capacitors and Supercapacitors.

Characteristics	Battery	Capacitor	Supercapacitor

Specific-Energy (Whkg^1)	10 – 100	<0.1	1 – 10
Specific Power (W kg^{-1})	<1000	>10000	500 – 10000
Discharge Time	0.3 – 3h	10^{-6} to 10^{-3}	Sec – min
Charge Time	1 – 5h	10^{-6} to 10^{-3}	Sec – min
Coulombic Efficiency (%)	70 – 85	About 100	85 – 98
Cycle Life	About 1000	Almost infinite	>500000

A comparison between batteries and supercapacitors are shown in Table: 1.2.

Table 0.2: Comparison Between Batteries and Supercapacitors.

Parameters	Supercapacitor	Battery
Storage mechanism	Physical.	Chemical.
Power limitation	Electrolyte conductivity.	Reaction kinetics, mass transport.
Energy storage	Limited (surface Area).	High (bulk).
Charge rate	High, same as the discharge.	Kinetically limited.
Cycle-life limitations	Side reactions.	Mechanical stability, chemical reversibility.

1.4 Introduction of Ferrites

Magnetic oxide Fe_2O_4 (Magnetite) was the first magnetic material ever discovered. The most important class of magnetic minerals are ferrites, which are used for a variety of purposes. They can be used in transformers, memory chips, antenna rods, inductors, and other devices. They have recently been used in sensors, green anode materials, and medication delivery. The three most important properties of ferrite are low dielectric losses, low eddy current, and high electrical resistivity. Ferrites are widely used in computers, microwaves, high frequencies, magnetic freezers and supercapacitors [16].

1.4.1   History of Ferrites

The history of (magnetic) oxides started many years ago with the discovery of stones that could pull iron. The Magnesia region, which gave magnetite (Fe_2O4) its name, is where these stones were most frequently found. Du-Bois (1890) conducted the first magnetic investigation of magnetite. Hilpert synthesized the first ferrites in 1909, and their typical formula is $MOFe_2O_3$. The letters M and O in this equation stand for divalent metal ions and oxygen atoms, respectively. In the first X-ray study of magnetic particles, Barth and Posnjak discovered an inverted spinel structure. The first workable modern ferrite was created in 1946, but early navigators used magnetite to locate magnetic north. For the ancients, magnetite was originally used to make lodestones. Verwey proved that the electron hopping between Fe_2 and Fe_3 ions is the main process behind the electrical conductivity of ferrites. It is known that ferrites with an inverted spinel structure are ferrimagnetic, while nonmagnetic ferrites have a normal spinel structure. Ferrites find utility in biosensing, medication delivery, and other biomedical fields. In more recent studies, wet chemical procedures are often used to produce nanoparticles of different ferrites. Several studies have looked into the connection between high dielectric constant and high ferrites conductivity [17].

1.4.2   Classification of Ferrites

Two main categories of Ferrites are : soft and hard ferrites, owing to their distinct characteristics and wide range of uses.

1.4.2.1 Soft Ferrites

Soft ferrites can be magnetized by placing them in magnetic field. They will only stay magnetized when the external magnetic field is present . Soft ferrites have very low coercivity and hysteresis loops, suggesting that the material's magnetization may change direction quickly and with little energy expenditure [18]. Soft ferrites exhibit reduced eddy current losses due to their higher intrinsic resistivity in comparison to other materials. As a result, they work better with other magnetic materials. An ideal ferrite should include:

- High permeability
- Negligible hysteresis loss value
- High saturation magnetization
- Low coercivity [19].

Hard Ferrites

Hard ferrites are stable and magnetic in nature. They are referred to as "Ceramic Magnets." Hard ferrites retain their magnetization even after the applied field is removed. They have high amounts of hysteresis loops and coercivity. Hard ferrites are composed of iron and oxides of barium or strontium. They can withstand magnetic fields stronger than those of iron because of their high magnetic permeability. Because ferrites are an extremely cheap raw material, they are widely used as permanent magnets [20].
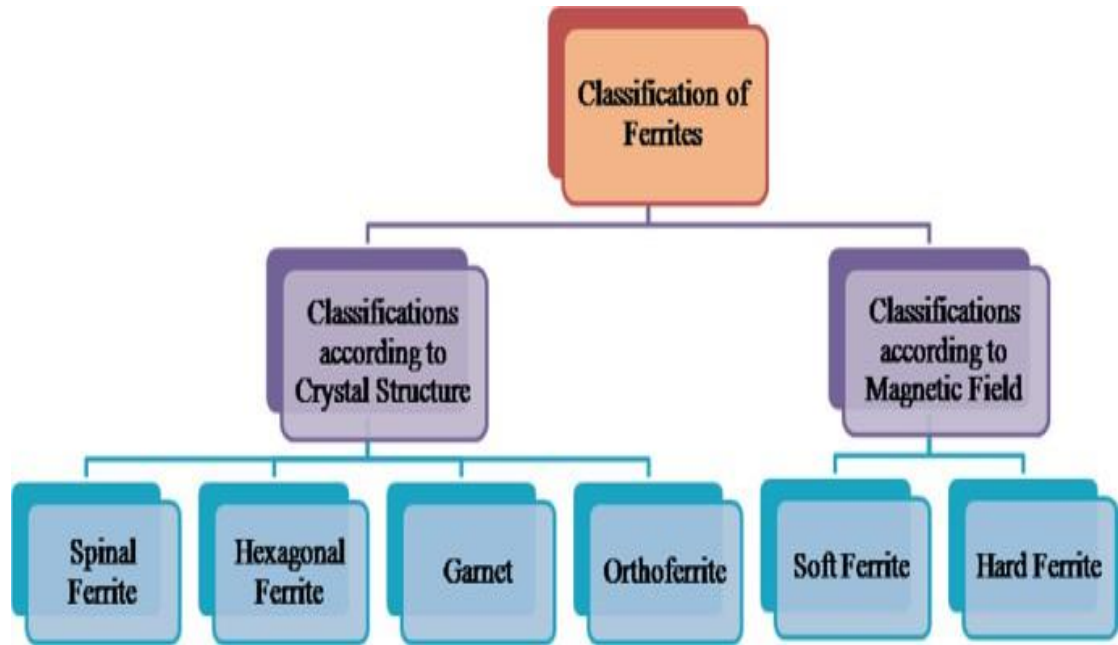
Figure 0.4: Classification of Ferrites

1.4.3 Types of Ferrites

Ferrites are classified into two groups. Ferrites with hexagonal and cube shapes.

1.4.3.1 Cubic Ferrites

Cubic ferrites are further divided into two types: (a) spinal Ferrites, (b) garnet Ferrites.

1.4.3.2 Spinal Ferrites

Spinal Ferrites have two sites : octahedral (B) and tetrahedral (A) sites. These Ferrites are flexible in nature. Low magnetic loss and high electrical resistance are characteristics of spinel ferrites[21]. Spinel ferrite nanomaterials, or SFNs, have unique properties and can be applied to an extensive range of applications. These include high-density gas sensors, catalysts, data storage, rechargeable batteries (like lithium batteries), magnetic bulk cores, magnetic fluids, microwave absorbers, information storage systems, supercapacitors and more. Spinel ferrites (SFs) typically have the chemical formula MFe_2O_4, where M stands

for Co, Fe, Mn, Ni, Cu, Co, Mg and Zn. These ferries have the same cubic symmetry as the mineral spinel [22]. Other trivalent ions such as Al^{3+}, Cr^{3+}, Ga^{3+}, etc., or a combination of divalent and tetravalent ions are used to replace iron ions. SFs are super paramagnetic (SPM) at the nanoscale, with a diameter of less than or equal to 20 nm. Every time, the metal cations at both sites are selected with the intention of filling areas where variables like the energy of stabilization, ionic radii, interstitial site size, and their synthesis reaction circumstances might have a significant influence [23].

1.5 Crystal Structure and Properties of Spinal Ferrites

The standard formula for configuration of spinel ferrites MFe_2O_4, which is formed from ($MgAl_2O_4$). In this formula, trivalent "Al" is substituted with Fe or a combination of Fe and other trivalent ions, and M denotes a divalent metal ion. One possible modification would be to add ions of Mn^{2+}, Ni^{2+}, Co^{2+}, Fe^{2+}, Zn^{2+}, or a combination of these ions to spinel ferrites in place of the divalent Mg^{2+} ions. Iron (Fe), iron in a high-spin state (Fe), nickel in a high-spin state (Ni), cobalt (Co), manganese (Mn), and iron (Fe) all produce unpaired electron spins. The tetrahedral holes of spinel ferrites are occupied by A cations in an eighth of the total number of holes, while the octahedral holes are occupied by B cations in half of the total number of holes. This is known as the cubic close-packed (FCC) oxide structure (O) [24].

If the B cation resides in one eighth of the tetrahedral   holes, one fourth of the octahedral sites, and the remaining one fourth, it is known as the inverse spinel structure.
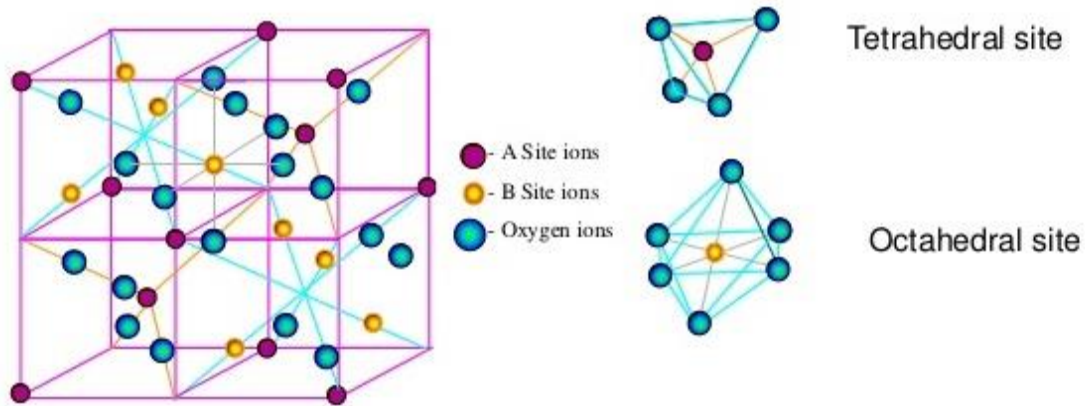
Figure 0.5: Unit Cell of Spinal Ferrite.

Each unit cell in the intricate structure of spinel ferrites is composed of eight molecules. There are two distinct types of sites in the FCC lattice of the 32 larger oxygen ions. The smaller ions (metals) occupy the interstitial gaps, which are of two types. One is tetrahedral [A]sites. 64 tetrahedral sites are surrounded by four oxygen ions. Because the oxygen ions are arranged around its corners, the second site is referred to as an octahedral [B] site. In total, there are 32 octahedral sites.

1.5.1   Types of Spinal Ferrites

Spinal structure has three types:

- Normal Spinal
- Inverse Spinal
- Random spinal

1.5.1.1 Normal Spinal Ferrites

The spinel is normal if the octahedral (B) site contains only one kind of cation. Eight divalent metal ions occupy the A sites, and sixteen trivalent iron ions sits at B sites.

12

1.5.1.2 Inverse Spinal Ferrites

The trivalent ions are located on sites A and B in an inverted spinel ferrite crystal lattice, while the divalent ions are exclusively found on site B.

Normal and Inverse Ferrites are shown in Figure: 1.6 [3].

1.5.1.3 Random Spinal Ferrites

Divalent metal ions are found on site A of a crystal lattice while trivalent metal ions are found on site B in typical ferrites. The ions in the A and B sites are distributed randomly in random spinals [25].
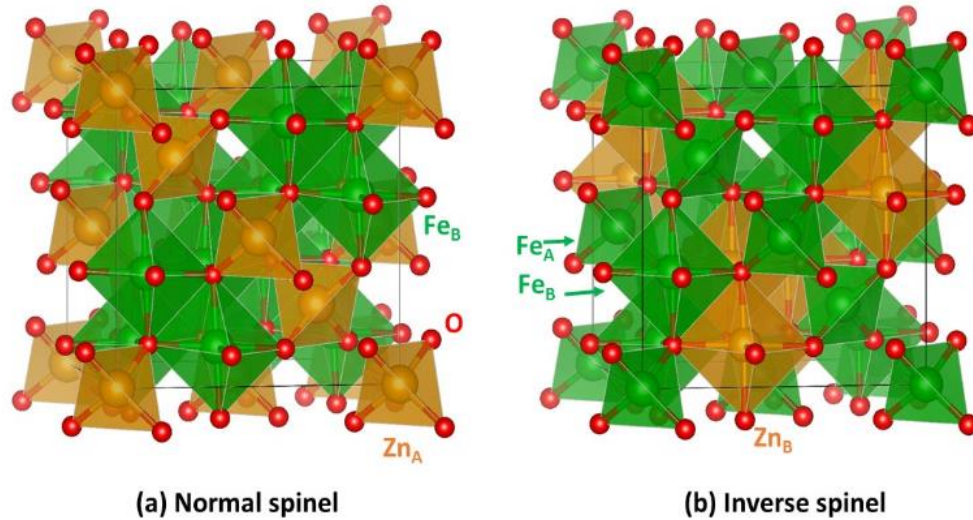
Figure 0.6: Atomic Structure of the Zinc Ferrite with (a) normal and (b) inverse Ferrite [3].

1.5.2 Garnet Ferrites

The garnet was discovered in 1957 by Geller and Gilleo. Eight formula units of $M_3Fe_5O_{15}$, where M is a trivalent rare earth ion like Y, Gd, or Dy, are found in the unit cell of a pure Iron garnet. Ferrites are unique translucent ceramics with a magnetic field. In magneto optical technology, they are useful. Garnet ferrites are composed of three sub-lattices. There are eight formula units, or 160 atoms, in a cubic unit cell. The edges of the cubic cell measure roughly 12.5A in length. Three interstices are occupied by metal cations in an array of 96 oxygen ions [26].

1.5.3 Ortho Ferrites

These ferrites are utilized in electrical circuits, magnetic field sensors, optical networks, mechanical quantities, and communication systems due to their high domain wall motion velocities.

1.5.4   Hexagonal Ferrites

They were first shown to have strong coercive characteristics in 1952 and are now frequently employed as permanent magnets. Permanent magnets are one of their common uses. and possess strong coercive abilities. Hexagonal ferrites have been studied and advanced at the Philips laboratory located in the Netherlands. Hexagonal ferrites have a significant uniaxial magneto crystalline anisotropy, which makes them useful in permanent, hard magnets. The letters M, W, Y, and Z stand for four distinct types of hexagonal ferrites with the general formula $MO_6Fe_2O_3$. M could be Pb, Sr, or Ba. Because of the challenge of merely shifting the magnetization's direction, they are tough ferrites [27].

1.6 Application of Ferrites

Because of their great resistance, superior magnetism properties, low cost, and ease of synthesis, ferrites are thought to be superior magnetic materials than pure metals. Soft ferrites can be utilized as transformer cores primarily for a) telecom computers, b) televisions, and c) medical and industrial electronics. Hard ferrites can be employed as permanent magnets in e) micro motors and loudspeakers etc. [28].

1.6.1   Magnetics Sensor

Magnetic sensors use ferrites with a clear and accurate Curie temperature to control temperature. In position and rotational angle sensors, ferrites are employed.

1.6.2   Magnetic Shielding

Radar-absorbing paint contains ferrites to make the submarine's aircraft unidentifiable to radar.

1.6.3   High density Optical Recordings

Spinel writing is used as thin films to produce media that can be repeatedly written on and read at blue wavelengths. These non-stoichiometric metastable ferrites are transformed into room-temperature corundum phases by means of lasers. The readout process is made simpler by the different optical indices of these locations that are being altered.

1.6.4   Pollution Control

Many Japanese locations use precipitations of ferrite precursors to filter contaminants like mercury out of waste streams. After this, these ferrites and the pollutants can be separated magnetically [29].

1.6.5   Ferrites in Entertainment Industry

Televisions and radios both use ferrites. Deflection yokes, flyback transformers, and SMPS transformers for power applications are among the uses for them. Ferrites have recently been used in

- Chokes, lighting bursts, and HE power supplies.
- TVs and monitors as circuits for magnetic deflection
- Frequency selective circuits as inductors and tuned transformers.
- Storage devices for recording heads.
- Matching devices as pulse and wideband transformers.
- VCR as spinning transformers [30].

1.6.6   Ferrite Electrode

Ferrites are used as electrodes because of their acceptable conductivities and strong resistance to corrosion.

1.7 Aims and Objectives

- Synthesize electrode materials of composition $ZnFe_2O_4$, $Zn_{0.5}Mg_{0.5}Fe_2O_4$, $Zn_{0.5}Co_{0.5}Fe_2O_4$ and $Zn_{0.5}Mg_{0.25}Co_{0.25}Fe_2O_4$ using coprecipitation.

- To characterize synthesized material various techniques will be employed such as X-ray diffraction, Fourier transformed infrared spectroscopy and Scanning electron microscopy.

- Application testing of synthesized electrode material will be done by cyclic voltammetry, electrochemical impedance spectroscopy and galvanic charge discharge.

1.8 Techniques for the Synthesis of Electrode Materials

Two methods are employed in the fabrication of nanostructures and nanomaterials. The first, a top-down approach, begins with bulk materials and progresses towards the nanoscale. Conversely, the bottom-up approach involves transforming atoms, molecules, or clusters into crystallites through nucleation, followed by the generation of particles via growth processes. This method encompasses compaction of powder aerosols and various chemical techniques. Notably, most oxide nanoparticles are produced using bottom-up methodologies [31].
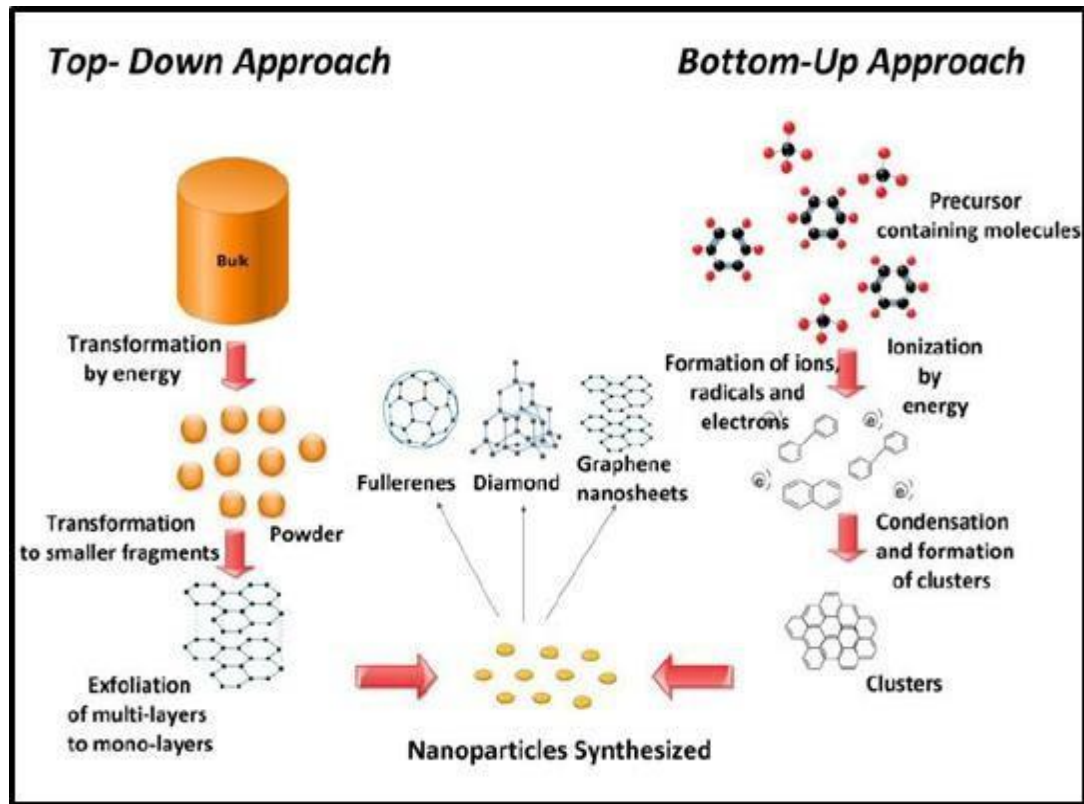
Figure 0.7: Top Down and Bottom-Up Approach for Nanoparticle Synthesis.

1.8.1   Top-Down Approaches

Mechanical or chemical energy is used to break down large materials into smaller parts. This technique includes:

- Etching, ball milling, and sputtering are larger scale designs which are all subsequently scaled down to the nanoscale.
- Lithographic procedures.

The above methods are cheap, yet it takes a while to produced and are inefficient for larger scale production [32].
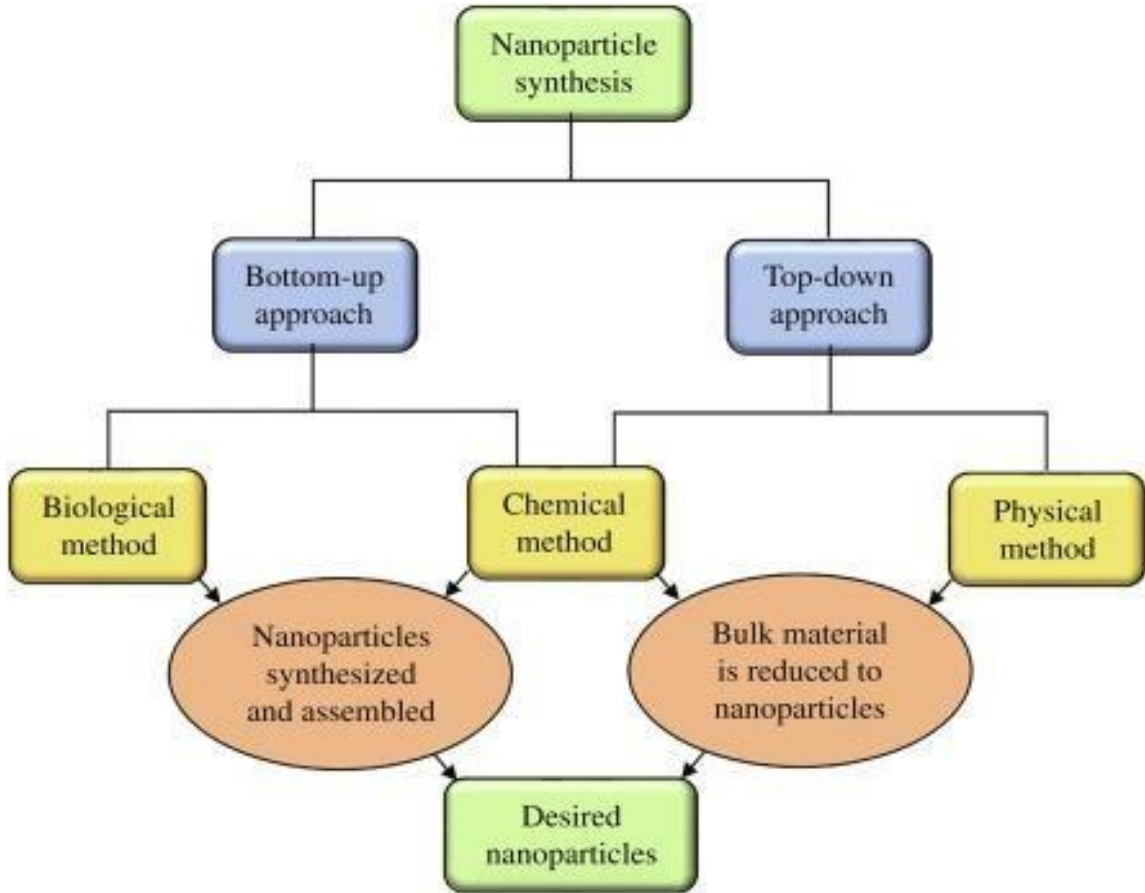
Figure 0.8: Flow Chart of the Synthesis of Nanoparticles.

1.8.2   Bottom-Up Approach

These cost-effective methods begin with atoms or molecules and build up to nanostructures through chemical processes. Examples include the Sol-gel method, Microemulsion method, Co-precipitation technique, Gas condensation process, Hydrothermal method,

Solvothermal method, Sono-chemical method, and synthesis of combustion flames [33, 34].

1.8.3   Sol-gel Method

In this process, precursors are combined to form a solution through hydrolysis, which is subsequently converted into a gel via dehydration in a liquid at a low temperature. This method employs conventional nanotechnology, as all gel products include nanoparticles or nanocomposites. Despite being straightforward and reasonably priced, this approach ensures a very high degree of purity [35].

High homogeneity is achieved with constant stirring. During the procedure, low temperatures are employed. This method has several uses in the fields of electronics, optics, and energy, but it also has advantages such challenging porosity optimization and weak bonding [36].
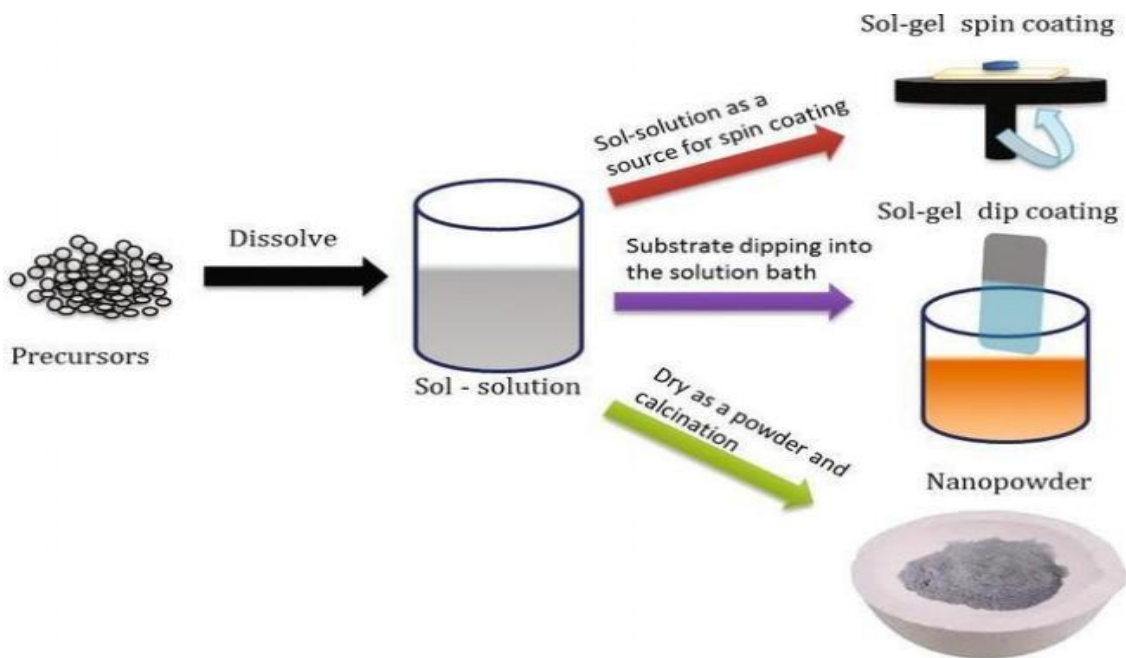
Figure 0.9: Solgel Process.

1.8.4   Micro Emulsion

According to the current study, binary phases are typically formed by combining stable isotropic liquid mixtures of oil and water surfactant. The resulting combination is diverse yet has a distinct morphology. The aqueous phase can contain a wide variety of components, including salts and other substances, while the oil component of the medium may possess complex properties. This material is a mixture of various olefinic chemicals and hydrocarbon molecules. The accompanying phase is usually composed of either water or oil, while the aqueous phases consist of both metal salts and surfactants. Two types of microemulsions are: direct microemulsions , where oil is dispersed within water, and reverse microemulsions , where water is dispersed within oil. The advantage of this method is that the distribution of the pore size is favorable, scaling up and production is simplified as there is low energy demand but surfactant removal is a challenging task [34].
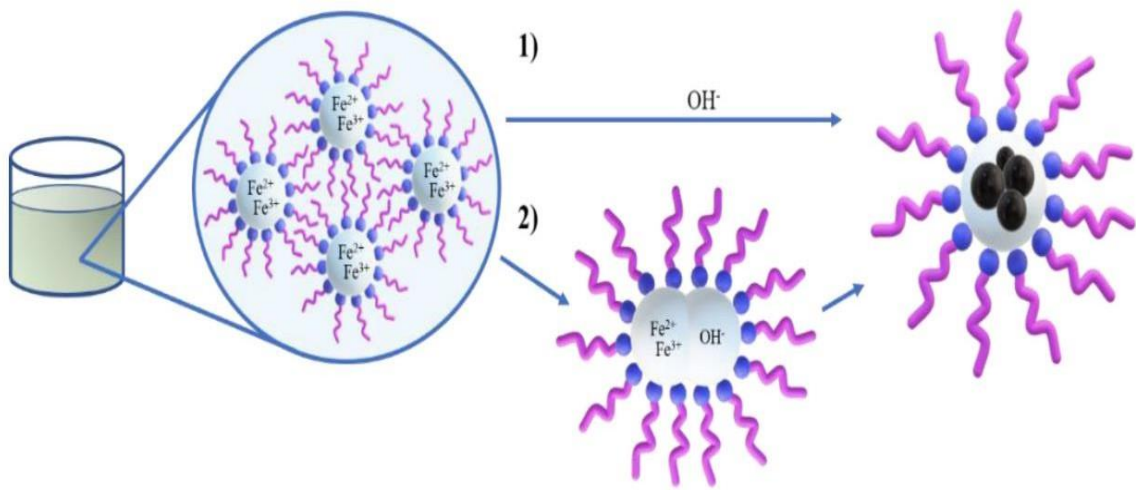
Figure 0.10: Microemulsion.

1.8.5   *Hydrothermal Synthesis*

The solvothermal approach is the most environmentally friendly and cost-effective technology because it can use either aqueous or non-aqueous solvents and provides good

control over particle size distribution. Using a heated solvent like n-butyl alcohol, in which the precursor is dissolved, can create gentler reaction conditions compared to water[35]. When water is used as the solvent, this method is called hydrothermal. Chemical reactions in these processes require specific temperature and pressure conditions.

Solvothermal synthesis has been employed in laboratories to produce nanostructured materials such as carbon nanotubes, graphene, and titanium dioxide. When water is used as the solvent , the method is identified as hydrothermal, and when another solvent is used, it is referred to as solvothermal.
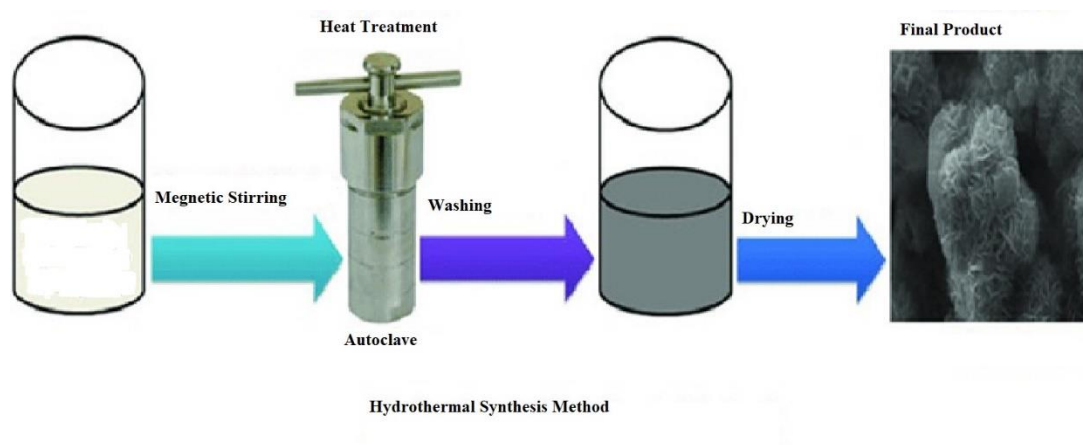
Figure 0.11: Hydrothermal Reactor.

Advantages

Morphology can be controlled easily and precisely by adjusting time, temperature, solvent concentration, and type.

Disadvantages

- The need of expensive autoclaves
- Safety concerns during the reaction process
- Inability to observe the reaction process[36].

1.8.6   Chemical Coprecipitation

The co-precipitation method is a well-established technique for producing nanoparticles on a nanoscale. It is straightforward, cost-effective, practical, and efficient, enabling the rapid production of pure, high-volume, and uniform ferrites. This method involves converting various salts such as sulfates, nitrates, and chlorides into oxide nanoparticles by precisely controlling the pH through the addition of NaOH. Following this, the sample undergoes centrifugation. The initial pH of the precursor significantly influences the particle size after the processes of drying, milling, and calcination are completed [37].

The molarity of the chemicals also affects particle size. Chemical concentration influences both reaction rates and transport processes. The crystallinity of the particles is determined by the reaction rate and the presence of contaminants. Parameters such as growth rate, nucleation, and supersaturation impact particle shape and size. High supersaturation results in smaller particle sizes. Since NaOH is used for precipitation, appropriate pH and temperature conditions are required [38]. An increase in temperature of 20 to 100 degrees
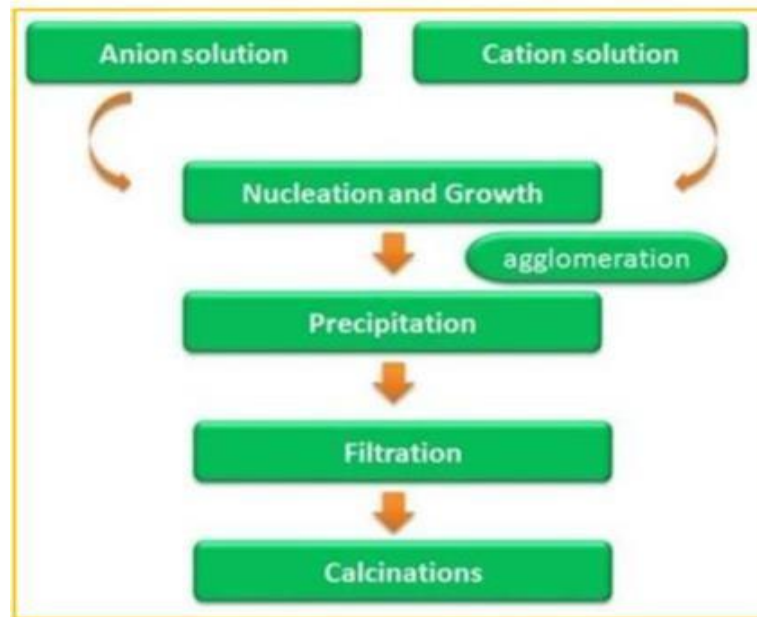
Figure 0.12: Chemical Coprecipitation.

Celsius significantly accelerates the formation of ferrites particles. This energy is produced by the reactants' heat.

1.8.6.1 Rate of Reactant Building

Rate of reactant building is crucial for the growth of nanosized particles and has a major effect on particle size. The co-precipitation is carried out by two processes: nucleation, which includes the creation of crystallization centers, and the subsequent development of these nuclei. Smaller, less dispersed particles form when the growth rate is moderate, and the nucleation rate is high. Nonetheless, large particles form when the growth rate exceeds the nucleation rate [39].

1.8.6.2 Role of Anion

The kind of anion and metal utilized in the co-precipitation method affect the properties of ferrites. One potential source of anions is metal ion solutions in the form of salts. It is recommended to use metal salt for the best possible outcomes. Perhaps the most often used metal salts are sulphates, nitrates, or chlorides.

1.8.6.3 Effect of pH

"pH" plays a important role in the formation of particles with controlled size and shape. The growth rate is minimal at low pH values and becomes more significant as pH rises. This is because the time required to create the product is shortened when the pH rises.

1.8.6.4 Heating Period After Coprecipitation

Concentrations of 0.2–0.4 moles/l are frequently employed to produce ferrites nanoparticles to create a non-viscous initial suspension of particles, which is beneficial for the better mixing of reacting volume.

1.8.6.5 Duration of Heating After Coprecipitation

After the co-precipitation process is finished, annealing is required. The degree and duration of heating are critical for achieving the required size and shape of the particles. **Pros:** This approach is environmentally sustainable. It is reasonably priced.

Cons: It is difficult to manage size distribution and create poor-quality crystals [40].

1.9 Synthesis of Ferrites via Coprecipitation

All four composites $ZnFe_2O_4$, $Zn_{0.5}Mg_{0.5}Fe_2O_4$, $Zn_{0.5}Co_{0.5}Fe_2O_4$ and $Zn_{0.5}Mg_{0.25}Co_{0.25}Fe_2O_4$ are synthesized using coprecipitation. It is a widely used method for creating ferrites, magnetic materials made of iron oxides and other metal components. This process has a number of benefits that make it a suitable choice for creating ferrites with desired characteristics. It guarantees control over the nucleation and growth processes, as well as an even distribution of metal ions throughout the solution. When compared to other techniques, coprecipitation can frequently be carried out at comparatively low temperatures, which lowers energy consumption and equipment needs. Additionally, this can stop unintended phase shifts from happening at higher temperatures. It works well for both industrial production and laboratory study, a feasible and profitable method of making ferrites. environmentally friendly by reducing the usage of dangerous chemicals and utilizing water as a solvent.

1.10   Characterization of Ferrites

Characterization will involve a range of techniques to confirm the formation of (a) $ZnFe_2O_4$ (b) $Zn_{0.5}Mg_{0.5}Fe_2O_4$ (c) $Zn_{0.5}Co_{0.5}Fe_2O_4$ (d) $Zn_{0.5}Mg_{0.25}Co_{0.25}Fe_2O_4$

1.10.1 Structural Analysis

To ascertain the crystal structure of the nanoparticles and validate their composition as (a) $ZnFe_2O_4$ (b) $Zn_{0.5}Mg_{0.5}Fe_2O_4$ (c) $Zn_{0.5}Co_{0.5}Fe_2O_4$ (d) $Zn_{0.5}Mg_{0.25}Co_{0.25}Fe_2O_4$ X-ray diffraction (XRD) will be employed.

Evaluation of surface morphology , shape and size of the nanoparticles is done using scanning electron microscopy.

1.10.3   Chemical Composition

1.10.3   Chemical Composition

Elemental composition of the nanoparticles, and verifying their purity and composition will be studied using Energy-dispersive X-ray Spectroscopy (EDS).

Surface Chemistry

The surface chemistry will be investigated using Fourier-transform infrared spectroscopy (FTIR) , which will verify the existence functional group.

1.11   Deposition of Electrode ink on Nickle Foam

Electrode ink will be made of synthesized materials using a binder and then deposited onto Nickle Foam which work as working electrode to gauge and compare the electrochemical properties of all four materials [41].

1.12   Electrochemical Properties

Three types of testing will be utilized to study electrochemical properties of the synthesized material.

1.12.1   Cyclic Voltammetry

1.12.1   Cyclic Voltammetry

It recognizes and describes the electrochemical processes that take place at the electrode surface. By giving details on the oxidation and reduction potentials, CV aids in the understanding of the redox behavior of materials. CV is essential for testing and assessing new electrode materials because it allows comparison of the electrochemical performance of various materials under similar conditions. CV is reasonably simple to perform and only requires standard electrochemical equipment. For supercapacitors, CV can measure the

capacitance of the electrode material by analyzing the area under the CV curve. It may be applied with different kinds of electrodes and in aqueous and non-aqueous conditions. Cyclic voltammetry is a vital tool in research and development, especially in the areas of batteries, fuel cells, and supercapacitors, as it offers thorough information about the electrochemical characteristics and behavior of materials.

1.12.2 Electrochemical Impedance

EIS is a non-destructive method that offers a thorough comprehension of the electrochemical processes and material properties. EIS is used to investigate the diffusion mechanisms, internal resistance, and charge transfer procedures in batteries and fuel cells. EIS can provide comprehensive details regarding the kinetics of electrochemical processes, including charge transfer resistance, double-layer capacitance, and reaction mechanisms, by analyzing the electrodes' impedance.

1.12.3 Galvanic Charge Discharge

To comprehend energy storage, stability and longevity are assessed through multiple charge discharge cycles. To evaluate the effectiveness of the charge-discharge process, compute the ratio of discharge capacity to charge capacity. Examining electrode behavior at various current rates in order to comprehend how it behaves under various operational scenarios.

1.13 Objectives of Study

- To study the electrochemical properties of the (a) $ZnFe_2O_4$ (b) $Zn_{0.5}Mg_{0.5}Fe_2O_4$ (c) $Zn_{0.5}Co_{0.5}Fe_2O_4$ (d) $Zn_{0.5}Mg_{0.25}Co_{0.25}Fe_2O_4$.

- In order to offer a thorough description of the synthesized nanoparticle's morphological, structural, and chemical characteristics along with capacitance, impedance, and discharge time.

- To find a suitable material by comparing electrochemical properties of all four materials synthesized.

CHAPTER 2:   LITERATURE REVIEW

2.1 Ferrites for Supercapacitors

Spinal ferrites are abundant and low cost and versatile metal oxides with good magnetic and electronic properties Spinal ferrites, Gadolinium doped bismuth ferrites and transition metal substituted manganese ferrites have shown great promise as electrode material for supercapacitors. These ferrites have unique structure, controlled pore size distribution and exhibit good electrochemical performances i.e. high specific capacitance [42-45]. Furthermore, it has been demonstrated that silver spinel ferrite and its composites, which have high specific capacities and power densities, are efficient electrode materials for supercapacitors [46]. Transition metal oxides and hydroxides (Ni, Co, Ru, etc.) have theoretical specific capacitance (SC) values more than 1000 F/g , and they are studied as potential active materials for supercapacitors. Still, there is a lot of space to improve capacitive values of these [41].The ability of ferrite nanostructures to facilitate rapid and reversible redox reactions at the electrode and electrolyte interface is crucial for the effective storage of charges in supercapacitors. All things considered, ferrites offer a viable path towards the creation of high-performing supercapacitors with improved power and energy densities. The introduction of alkali metals like lithium into Zn ferrites via Sol-gel methods significantly improves their electrochemical properties, leading to specific capacitance values as high as 898 F/g and excellent cycle life, making them promising materials for supercapacitor applications [47].

Furthermore, $BiFeO_3$ crystal's ability to store electrochemical energy is improved by the creation of oxygen vacancies , which create advantageous ion transport pathways and produce a large specific capacitance of 461.9 F/g and high cycling stability after 2,000 cycles[43]. Additionally, the synthesis of transition metal ferrites, such as $CuFe_2O_4$ and $CoFe_2O_4$, as electrode materials has exceptional cycling stability and specific capacitance values of up to 893 F/g, highlighting their potential for use as supercapacitor electrodes [48]. All of these studies demonstrate how ferrites, by enhancing specific

capacitance, cycle life, and overall electrochemical performance, have played a major role in the advancement of supercapacitor technology.

$ZnO@CoFe_2O_4$ and $CoFe_2O_4$ nanocomposites with high surface area and electrical characteristics are promising candidates for various applications. Using hydrothermal method, these two nanocomposites Electrodes on nickel foam were created for high performance electrochemical supercapacitor applications. The $ZnO@CoFe_2O_4$ nanocomposite electrode demonstrated a high specific capacitance of 4050.4 F/g at 10 $mAcm^{-2}$, along with a high energy density of 77.01 Whk/g in a 3 M KOH solution. After 1000 cycles, this electrode showed attractive cycling stability and a specific capacitance of about 90.9% capacity retention. Conversely, the $ZnO@CoFe_2O_4$ nanocomposite electrode exhibited a higher specific capacitance of 3499.9 F/g and cycling stability 50.07% than the $CoFe_2O_4$ electrode. These findings demonstrate the electrode potential of $ZnO@CoFe_2O_4$ nanocomposite electrodes as electrodes for high energy density storage systems [49].

BTMO-based electrodes $ZnFe_2O_4$ZnFe2O4-rGO electrode shows the capacitance of 1419 F/g. It has been shown that when rGO is added to the electrode structure, the stability rises to 94% over 5000 cycles and the discharge time is noticeably longer with rGO electrodes. So, because of their low cost and relatively high efficiency, the suggested materials hold great promise for supercapacitor electrodes [50].

Different compositions of $ZnFe_2O_4$ZnFe2O4-based nanofibers were produced by electrospinning, employing PVP as the polymer and ferric and zinc acetonates as metal oxide precursors. It has been shown that various compositions have an impact on the electrochemical and super capacitive characteristics for supercapacitor applications. Fe_2O_3–$ZnFe_2O_4$ZnFe2O4 had the highest specific capacitance , 590F/g at a scan rate of 5 mVs^{-1} as shown by the Cyclic Voltammetry curve. ZnO–$ZnFe_2O_4$ZnFe2O4 shows specific capacitance of 490 F/g, while $ZnFe_2O_4$ZnFe2O4 has a capacitance of 450 F/g. This can be explained by Fe_2O_3's pseudocapacitive characteristic. Even after 3000 cycles, all of the electrodes showed good cycle stability , with a capacitance retention of roughly 92% to 95%. These $ZnFe_2O_4$ZnFe2O4 based nanofibers are interesting electrode materials for

supercapacitors and other energy storage applications because of the easy and affordable electrospinning technique and the outstanding results obtained from these electrodes [51].

$ZnCo_2O_4$ is a spinel, with trivalent Co ions occupying the octahedral sites and Zn ions occupying the tetrahedral sites in the cubic spinel structure. Ionic charge builds up in the double layer at the electrode-electrolyte interface of these porous electrodes, storing energy. $ZnCo_2O_4$/CNF demonstrates low impedance and high specific capacitance contrary to pure metal oxide nanocomposites. When CNF was added to metal oxide, the electrode's internal resistance decreased, increasing the specific capacitance. $ZnCo_2O_4$/CNF-based supercapacitors demonstrated a specific capacitance of 77 F/g [52].

NiFe2O4 nanoparticles synthesized by solgel process, may find application in energy storage devices such as supercapacitors. An average crystalline size of about 40 nm and a micro-strain of roughly -0.00346 were found by structural analysis. FESEM surface morphology tests validated the samples' nanoparticle sizes. The synthesized materials' supercapacitive behavior was investigated electrochemically using cyclic voltammetry. The results showed that the maximam area was covered at a scan rate of 100 mV/s, with a specific capacitance of about 200 F/g. During the redox reaction, the maximum contribution of active ions was seen at lower scan speeds. An impedance analyzer was used to measure and examine electrical properties such as impedance, dielectric constant, dielectric loss, and AC conductivity. In light of the findings, NiFe2O4 is suitable for supercapacitor applications [53].

Synthesized nickel-zinc ($Ni_{0.5}Zn_{0.5}Fe_2O_4$) ferrite nanoparticles were examined for their surface area, composition, structural, morphological, and magnetic characteristics. Field-emission scanning electron microscopy and X-ray diffraction studies demonstrated that the nanoparticles size distribution and shape were uniform. The quality of the nanoparticles was verified by Fourier transform infrared spectroscopy, which revealed the absence of organic components. Superparamagnetic behavior was shown by magnetic study, with a saturation magnetization of 33.22 emu/g. The material's specific surface area, according to N2 adsorption–desorption experiments, was 42.26 m²/g. The efficiency of these nanoparticles as supercapacitors was demonstrated by electrochemical investigations;

cyclic voltammetry revealed a well-developed curve suggestive of stable and reversible redox behavior. Rapid potential shifts, stable plateaus, and general stability were seen in the charge-discharge behavior, indicating that it would be appropriate for quick cycles of charging and discharging. Nickel-zinc ferrite nanoparticles are good candidates for supercapacitors because they have favorable electrochemical properties and high energy storage efficiency. These nanoparticles may find a variety of uses in energy storage devices with additional integration and optimization [54].

Because of the facile adsorption-desorption of ions, the Zn-Co oxide electrode's 3-D shape linked to its high specific capacitance and strong cycling stability at varying Zn^{+2}/Co^{+2} mol ratios. All of the electrodes are nanoporous structures that offer effective ion transport channels, enhancing Supercapacitive performance. Excellent conductivity is ensured by the electrodes making direct contact with the nickel foam. Because of all of these factors, electrode deposited on synthetic nickel with varying morphologies show excellent promise as high-performance supercapacitor electrodes. The maximum specific capacitance of 1273 F/g at 50 mV s^{-1} scan rate is shown by the Zn-Co (1:2) oxide electrode synthesized at 180 °C. This is approximately 1.8 and 3.14 orders of magnitude greater than that of Zn oxide having capacitance of 405 F/g and Co oxide with capacitance of 705 F/g, respectively. At a scan rate of 100 mV s^{-1}, 92% of the capacitance was retained after 1000 cycles using this binary electrode. Investigating the Zn-Co oxide electrode's capacitance property at various Zn^{+2}/Co^{+2} mol ratios , the maximum specific capacitance was found at Zn^{+2}/Co^{+2} equal to 1:2 mol ratio [55].

CoFe2O4 nanoparticles with an average size of 23 nm and used to create an electrode that was altered for usage in supercapacitors. Cobalt ferrite offers substantial benefits in electrochemical energy storage due to its broad spectrum of oxidation states. At 0.6 A/g of current density, the produced electrode displayed a capacitance of 15 F/g. CoFe2O4 nanoparticle-based electrodes have a simple and affordable production procedure, which makes them highly promising for use in next-generation supercapacitors [56].

For supercapacitor electrodes, $NiFe_2O_4$ and $NiFe_2O_4$/rGO are also tested. $NiFe_2O_4$/rGO reaches a high capacitance of 584.63 F/g at the scan rate of 10 mV/s , three times more

than pure $NiFe_2O_4$. Moreover, compared to Ni Fe_2O_4, the $NiFe_2O_4$/rGO electrode exhibits a greater rate capability and cycling stability. After 2000 CV cycles, $NiFe_2O_4$/rGO exhibits a capacitance retention of 91%. This excellent performance can be attributed to the high surface area, synergistic impact between $NiFe_2O_4$ and rGO as well as between Ni/Fe ions, and electronic conductivity provided by rGO. This shows significance of $NiFe_2O_4$ as a cathode material for energy storage devices such as pseudo-capacitors [57].

Compared to monometallic oxides (Mn_xO_y or Fe_xO_y), $MnFe_2O_4$ electrodes exhibited a significantly higher pseudo capacitance and a faster redox reaction and has been utilized for its high specific capacitance. So, $MnFe_2O_4$ based materials and their interfacial electrochemical can be used for adaptable energy storage systems to satisfy various requirements of wearable and portable electronics [58].

It has been determined that MXene-Ferrite nanocomposites are suitable materials for photocatalytic and electromagnetic applications. Because of things like natural resonance, interlayer multireflection, eddy current loss, and dipole and interfacial polarization, the Ti_3C_2Tx/CNZFO/PANI composite performs better than other materials. The 2-weight percent Ti_3C_2Tx/NiZn composite exhibits a considerable increase in both electrical conductivity and magnetic saturation. Moreover, the BFO/MXene photocatalyst exhibits excellent efficiency. Ti_3C_2Tx/Fe3O4@C hybrids are readily fabricated and exhibit potent photocatalytic activity. At a frequency of 17.50 GHz and a thickness of 7.41 nm, these composites attain a maximum absorption bandwidth of 2.32 GHz with a minimum reflection loss (RLmin) of −69.86 dB. According to a review of MXene nanocomposites, composites containing ferrite show great promise for use in electromagnetic interference (EMI) shielding and pollution absorption applications [59].

$CuFe_2O_4$ /MXene nanohybrids were successfully synthesized at a reasonable cost. The resultant nanohybrids show great promise in the photocatalytic pathway for e$^−$-h$^+$ separation. The addition of $CuFe_2O_4$ to MXene is responsible for their exceptional photocatalytic performance and antibacterial activities. The creation of a cross-linked network, high surface area, and remarkable magnetic characteristics are facilitated by this inclusion. In 40 minutes, 94% of the methylene blue was degraded by the magnetically

separable CuFe$_2$O$_4$ /MXene nanohybrids, forming a new photocatalyst with significant reusability. These CuFe$_2$O$_4$ /MXene nanohybrids could find use in energy-related processes like electrocatalysis or hydrogen generation [60].

2.2 Current Challenges

Lithium-ion batteries and supercapacitors are commonly utilized in industries. However there exists a disparity between the two as supercapacitors lack energy density. The recent breakthrough involving MXene based anodes has enhanced energy storage and overall performance of supercapacitors. To further boost supercapacitance different ferrite materials are combined with MXene offering an energy source for portable and wearable electronic devices by facilitating greater surface area for redox reactions.

When compared to other materials utilized in supercapacitors, like carbon-based materials and certain metal oxides, ferrites usually have poorer electrical conductivity. This low conductivity may restrict the supercapacitor's charge-discharge speeds and lower its overall power density[61].

It is still unclear how long-lasting and electrochemically stable ferrite-based electrodes will be after numerous cycles of charge and discharge. Over time, ferrites may experience reduced performance due to structural changes or dissolution in the electrolyte [62]. The effective surface area available for electrochemical reactions is reduced when ferrite nanoparticles agglomerate. The capacitance and general performance of the supercapacitor may be negatively impacted by this aggregation [63]. It is difficult to design an electrode structure that maximizes ferrites electrochemical performance. Particle size, porosity, and the distribution of active ingredients are a few examples of factors that requires attention [64].Ferrites are frequently integrated with conductive materials like carbon nanotubes, graphene, or MXenes to expand the performance of ferrite-based supercapacitors. The technical difficulty of achieving a consistent and reliable integration remains a challenge [65]. It is important to carefully investigate whether different electrolytes are compatible

with ferrite-based electrodes. The overall stability and performance of the supercapacitor can be impacted by the interaction between the electrolyte and the electrode material [66].

Currently, a number of obstacles are preventing supercapacitors from being commercialized. The potential applicability of this sort of energy system is limited by the inadequate energy density of supercapacitors, which is a potential pitfall. Supercapacitor's high-power density and extended life cycle aren't enough to entice businesses and customers to completely replace batteries with them. The high cost of supercapacitors is another obstacle to their widespread use. Supercapacitors may store up to 20 times less energy at a given size or mass than lithium-ion batteries. The lack of supporting infrastructure is another difficulty for the nationwide implementation of supercapacitors. For instance, the markets for electric vehicles would profit immensely from the plethora of potential applications for supercapacitors. But before these cars can be commercialized, new charging stations must be installed around the country, which could take a few years to complete [2].

2.3 Future Direction

Researchers and industry professionals are working hard to find new uses for supercapacitors. "Volvo" created structural energy storage components that are lightweight and made of polymer resins and carbon fibers. The parts, which function like supercapacitors, weigh a lot less compare to typical batteries already seen in electronic cars. Furthermore, the energy storage components are easily moldable into the necessary shapes. Supercapacitive materials were used in place of the trunk lid and plenum cover on the Volvo S80 prototype in order to store brake energy. The notion of wearable electronics is gaining attraction as researchers incorporate supercapacitor technology into apparel. "Li" from the University of South Carolina designed a T-shirt with supercapacitor-like capabilities [2].

An area of research that is just getting started but has a lot of potential for use in energy storage , electromagnetic interference (EMI) shielding, and environmental remediation is the combination of MXenes with ferrites. A feasible strategy for improving the

performance of supercapacitors is to combine MXenes with ferrites, using special qualities of both materials. MXenes have a high electrical conductivity that makes fast electron transit possible, which is necessary for high-power supercapacitors. Their two-dimensional structure offers a lot of active sites for charge storage due to its vast surface area. MXenes interact with electrolytes more readily due to their surface chemistry, which improves electrochemical performance. They have mechanical flexibility, enabling them to create durable and flexible films that are well-suited for use in flexible supercapacitors [67, 68].

MXenes and ferrites can be physically mixed and then processed into composite electrodes. This approach is simpler but might require additional steps to ensure uniformity and good contact between the materials [69]. So, a composite of MXene with the ferrite which shows better results for supercapacitors can be made and tested for its capacitance, current density, and charge discharge. This might result as a reliable source for electrode material for supercapacitors.

CHAPTER 3: MATERIALS AND METHODS

3.1 Synthesis of Ferrite Nano Composite

The method used to synthesize nano particles is coprecipitation using molar ratio 1:2 [70]. The salts used are Zn $(NO_3)_2.6H_2O$, Fe_2 $(NO_3)_3.9H_2O$, Mg $(NO_3)_2.6H_2O$ and Co $(NO_3)_2.6H_2O$.

3.2 Synthesis of $ZnFe_2O_4$

Deionized water (150 ml for each) is used to mix salt of Zn and Fe_2O_4. This mixture is stirred until homogenized. Then heat this solution 50°C – 55°C. In another beaker NaOH solution is made by dissolving 18 g of NaOH salts in 150 ml of DI water. This solution is magnetically stirred and heated to 80 °C. When temperature of both solutions reached 80 °C, solution of NaOH is mixed immediately to the $Zn+Fe_2O_4$ solution. Heat this mixture for 45 minutes, then turn off the heating and continue stirring until the temperature decreases to 25 °C – 30 °C and the solution volume is reduced to 300-400 ml. Continue washing the mixture with distilled water until the pH is neutral (pH 7). Dry the mixture in an oven at 90°C overnight. Finally, crush it into a powder and anneal it in a muffle furnace for 4 hours at 610°C.

3.3 Synthesis of $ZnMgFe_2O_4$

For the doping of Mg in $ZnFe_2O_4$, Use 450 ml of deionized (DI) water to mix Zn, Mg, and Fe_2O_4 (150 ml of DI water for each). Stir the solution until it is homogeneous and then heat it to 50°C – 55°C. Prepare a sodium hydroxide solution by dissolving 18 g of NaOH in 150 ml of DI water , followed by magnetic stirring and heating to $80^{°C}$. When both solutions reach 80°C, immediately mix the NaOH solution into the $Zn_{0.5}Mg_{0.5}Fe_2O_4$ solution. Heat this mixture for 45 minutes, then turn off the heat and continue stirring until the temperature decreases to 25 °C – 30 °C and the solution volume is reduced to 300-400 ml. Continue washing the mixture with distilled water until the pH is neutral (pH 7). Dry the mixture in

an oven at 90°C overnight. Finally, crush it into a powder and anneal it in a muffle furnace for 4 hours at 610°C.

In this way all four samples are synthesized by the aforementioned method. Synthesized samples are.

- $ZnFe_2O_4$
- $Zn_{0.5}Mg_{0.5}Fe_2O_4$
- $Zn_{0.5}Co_{0.5}Fe_2O_4$
- $Zn_{0.5}Mg_{0.25}Co_{0.25}Fe_2O_4$

3.4 Samples preparation for XRD:

XRD analysis was done for the identification of crystal structure. In XRD testing sample is used in powdered form. A small amount is placed in the holder, then this holder is placed into the chamber. A heated filament is used to produce the electrons, which are then accelerated towards anode with the help of very high voltage. These highly accelerated electrons strike the metal target (generally Cu) and as a result, characteristic X-rays are produced. These characteristic X-rays are directed towards the sample by using different slits. These X-rays on striking the sample planes are diffracted at different angles and are detected by the detector. Diffracted X-rays from different planes produce constructive or destructive interference, and in case of constructive interference appear in the form of intensity peak in the XRD plot.

3.5 Samples preparation for FTIR:

To prepare samples for FTIR, pallets are made using a small amount of sample powder along with KBr by pressing into a thin pallet. Reason for using Potassium bromide (KBr) is that it is highly transparent in the mid-infrared region, making it an excellent matrix material for Fourier-transform infrared (FTIR) spectroscopy. This transparency allows infrared light to pass through the KBr without interference, enabling accurate analysis of the sample. Additionally, KBr has minimal absorption in the same region where many samples exhibit strong infrared absorption bands. This low absorption characteristic

ensures that the matrix does not overshadow or interfere with the absorption signals of the sample, making KBr particularly suitable for analyzing materials with prominent infrared absorption features. Its inert nature and ability to form homogenous mixtures with the sample further enhance its utility in FTIR spectroscopy, providing clear and reliable spectral data

3.6 Samples preparation for SEM:

Scanning electron microscope (SEM) was used to study the topography and microstructure of the developed foams. In scanning electron microscope, electrons are generated by heating of tungsten filament and are directed towards the specimen by using the anodic voltage and magnetic lenses. The electrons are charged particles and as they pass through the magnetic field they are deflected and point towards a point on the specimen. The SEM chamber is kept under vacuum conditions to avoid the splattering of electrons. To prepare sample for SEM, suspension of each sample was made by mixing a very minute amount of each sample powder into DI water in a vial and sonicate it for 4 hours in a sonication bath. Four glass slides are prepared of dimension 1×1 cm. The prepared suspension of each sample is dropped cast on glass slide and dried in vacuum oven to remove moisture. After drying the glass slides are coated with gold to make it conductive for SEM.

3.7 Sample preparation for Electrochemical Testing:

For electrochemical testing, electrode ink is prepared which is then deposited on Ni foam to work as a working electrode.

3.8 Electrode ink preparation:

Activated material (5 mg) is mixed with 300 micro litter of DI water and 200 micro litter of ethanol along with 20 micro litter of Nafion as a binder. This solution is ultrasonicated for 2 hours before dropped cast on Nickle foam.

3.9 Deposition of Synthesized Material on Ni Foam

The Ni foam substrates of dimension (1 × 1 cm²) were initially treated with a 0.5 M HCl solution, then washed and dried at 70°C for 4 hours. Next, the Ni foam pieces were immersed in a mixture containing 5 mg of the synthesized material, ethanol, DI water, and Nafion, and subjected to ultrasonication for 2 hours. Afterwards, the substrates were dried overnight at 60°C.

Once the Ni foam is treated and electrode ink is prepared, 20 micro litter of electrode ink is dropped cast on Ni form and placed it in vacuum oven for drying. After 10 minutes ink is again dropped on Ni foam so that maximum ink is loaded on Ni foam. The ink dropped should be done during sonication so that it does not settle down in bottom. Then this Ni foam is dried overnight to use as working electrode for electrochemical testing.

For electrochemical testing Gamry software is used in which first we activate the working electrode by giving some current then cyclic voltammetry, galvanostatic charge discharge and electrochemical impedance spectroscopy is performed using same software.

Figure 0.1: Synthesis of Ferrites Via Coprecipitation.

CHAPTER 4: CHARACTERIZATION TECHNIQUE

The $ZnFe_2O_4$, $Zn_{0.5}Mg_{0.5}Fe_2O_4$, $Zn_{0.5}Co_{0.5}Fe2O4$ and $Zn_{0.5}Mg_{0.25}Co_{0.25}Fe_2O_4$ produced were characterized using X-ray diffraction (XRD) spectroscopy with CuKα radiation (0.154 nm) from a Shimadzu Co. XRD-6000 instrument. The materials were examined at room temperature (RT) within the range of 10 and 80 in two theta range. The particle size of the material was determined using a Scanning Electron Microscope (HR-TEM), JEOL - JEM 2100. Fourier-transform infrared spectroscopy (FTIR) is employed to examine functional groups within the material, covering the range of 4000-400 cm^{-1}. Cyclic voltammetry , Electromagnetic impedance spectroscopy and Galvanic charge discharge performed to assess the specific capacitance, impedance, and discharge time.

4.11   X-Ray Diffraction Spectroscopy (XRD)

X-ray diffraction (XRD) stands out as a widely employed method for describing crystalline materials, owing to its remarkable efficacy. This approach offers thorough insights into structural deformations, crystal anomalies, average crystallite sizes, crystallographic alignments, and the degree of crystallization. Analyzing peak intensities entails evaluating the atom distribution within the crystal lattice. Consequently, X-ray diffraction data furnishes comprehensive details regarding the periodic arrangement of atoms within the material under examination.

When utilizing the powder diffraction method, two techniques can be employed to ascertain crystal size:

- The Debye-Scherrer Method
- The Diffractometer Method

4.1.1   *Working Principle of XRD*

For analysis, the powdered form sample is subjected to an X-ray beam and the rays are reflected from the plane of the crystal substance. Interference occurs only when the

incidence and reflection angles are the same. Bragg's law is given by.

$$2d\sin\theta = n\lambda$$

"n" is the order of interference, "d" is space between layers, θ is incidence angle, and λ is wavelength of X-ray of incident. Bragg's law states that an incident ray is reflected only when the path difference between a set of planes is $2d\sin\theta$. Here, "d" represents the distance between the planes. The condition required for constructive interference is that this path difference must be an integer multiple of the wavelength.
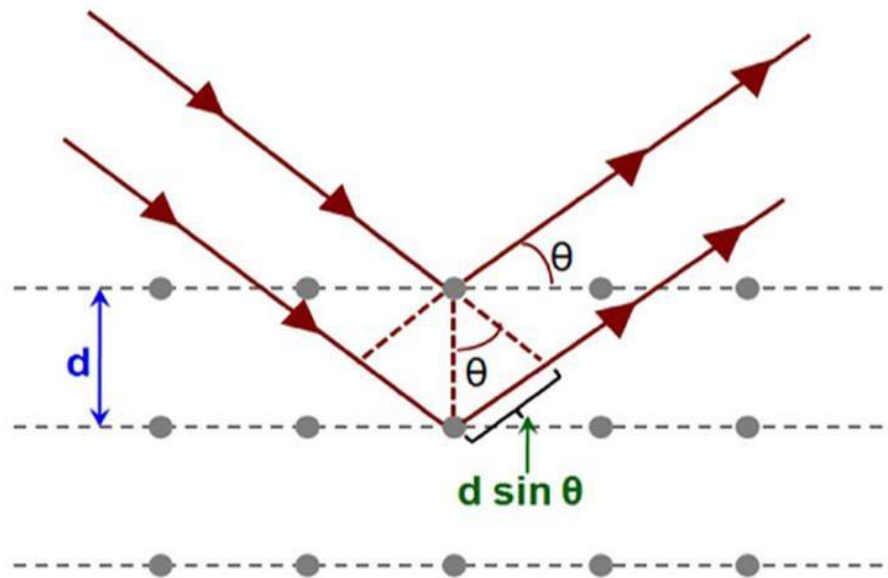
Figure 0.2: Incident X-Ray Beam Scattering.

Visible light cannot be employed because the above equation's criterion for reflection states that it can only occur when $0 < 2d$ [71]. Graphic representation of the working principle of XRD in Figure: 4.2. [1].
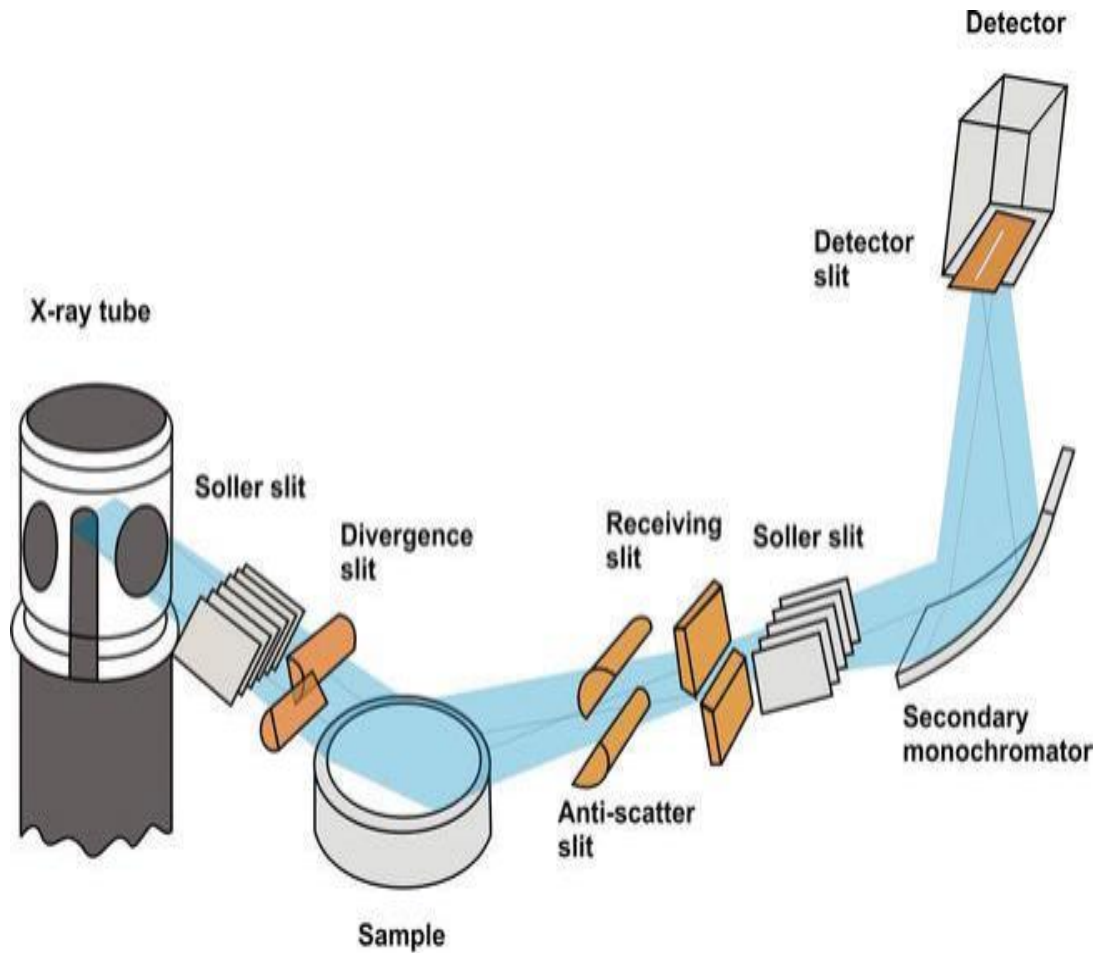
Figure 0.3: Working Principle of XRD [1]

4.1.2 Crystal Structure

Generally, three techniques are applied to analyze the crystal structure of synthesized material.

- Laue Method
- Rotating Crystal Method
- Powder Method

4.1.3 Laue Method

It is the original diffraction technique, derived from the first experiment by von Laue. This method involves white continuous light on a stationary crystal structure. The Bragg angle θ remains constant for each set of planes in the crystal. Only wavelengths that satisfy Bragg's law for specific θ and d values are diffracted. As a result, each diffracted beam has a different wavelength. This method includes analysis of the diffraction patterns to determine the crystal structure. This technique includes:

- Transmission Laue Method
- Back Reflection Laue Method

To collect the forward-diffracted beams for analysis using the transmission Laue method, the crystal is placed in front of the film. By sandwiching the film between the X-ray source and the crystal and allowing the incident beam to pass through a hole in the film , the backward-diffracted beams are captured in the back-reflection method.

4.1.4   Rotating Crystal Method

A single crystal is fixed on one axis, cylinder-shaped film is wrapped around it, and the crystal is spun in the chosen direction.

4.1.5   Powder Method

Powder diffraction is a highly effective method for characterizing samples, particularly using nano powder when a single crystal of adequate size is unavailable. The process involves crushing the sample into a fine powder. This powdered sample is then placed on a rectangular glass or aluminum plate. A monochromatic X-ray beam is directed at the powdered sample to analyze its structure. This technique is especially useful for assessing powdered samples using ARD 1S.
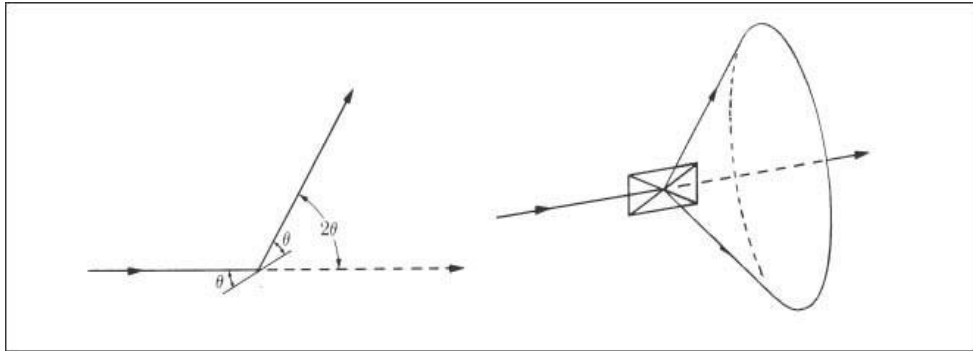
Figure 0.4: Diffracted Cones of Radiation Formation in Power Method.

The powdered sample is aligned to allow reflection at the correct Bragg angles. When the sample plane is rotated around the incident beam, the path of the reflected beam forms a conical surface. Although not all particles reflect across this surface, many will have the same reflections, with some satisfying Bragg's law. The interplanar spacing "d" can be calculated using the known values of the wavelength "λ" and the angle "θ".

4.1.6   Lattice Constant

The lattice constant provides a clear understanding of a crystal's unit cell structure. It refers to the dimensions of the cell, specifically the length of an edge or the angles between edges. This measurement is known as the lattice constant or lattice parameter in academic contexts. In crystallography, the lattice constant is a well-established term that denotes the fixed distance between lattice points.

Lattice constant calculations can be done by:

$$d_{hkl} = \frac{a}{\sqrt{h2+k2+l2}}$$

In above mentioned equation, lattice constant 1s "a" the wavelength of X-ray elation is 1.54 A° for Cuka, miller indices are "h, k, l" and diffraction angle is 0 radian or degree.

Crystallite Size

The experimentally discovered diffraction is identified and verified by comparison with JCPDS cards. Particle size mainly affects the structural characteristics. The Debye-Scherrer equation is used to analyze particle size. Peak width is inversely proportional to crystal size, which makes sense when considering the Debye-Scherrer equation , which is used to calculate particle size by utilizing the FWHM values of the peaks.

$$D = \frac{K\lambda}{\beta cos\theta}$$

λ represents the incident X ray wavelength , K is the Scherrer constant and θ is angle of diffraction whereas is full width half maximum [72].

4.2 Scanning Electron Microscopy

Scanning electron microscope (SEM) is used to examine the topography and
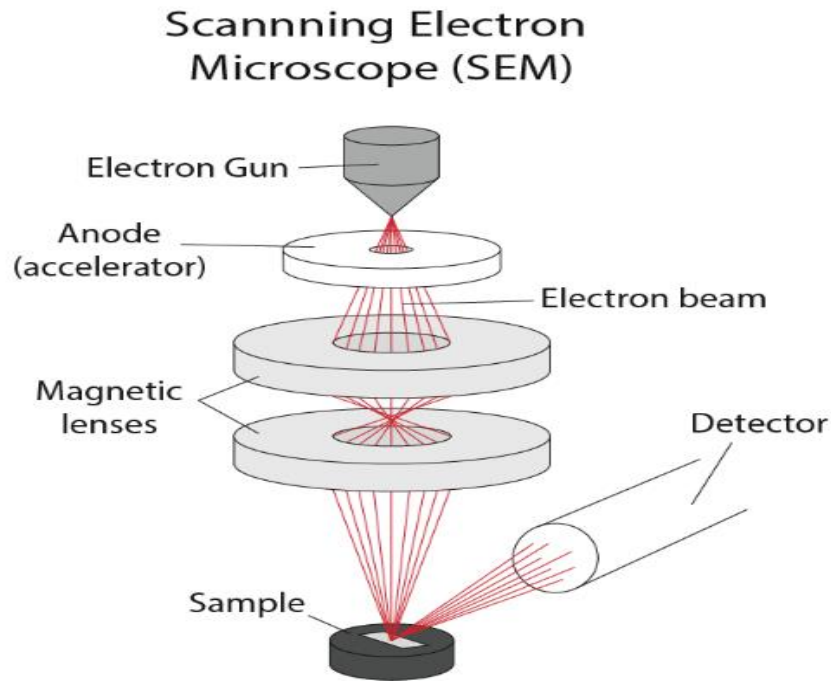
microstructure of the developed foams. In an SEM, electrons are produced by heating a tungsten filament and are directed toward the specimen using anodic voltage and magnetic lenses. As charged particles, the electrons are deflected by the magnetic field and focused on a point on the specimen. The SEM chamber is maintained under vacuum

conditions to prevent electron scattering. A general schematic illustrating the SEM's working principle is shown in the figure: 4.4.

The penetration of electrons into the sample surface is directly influenced by the provided voltage; higher voltage increases penetration. These electrons interact with the sample and eject specimen electrons. Depending on the voltage and penetration level, four different types of interactions occur, each requiring separate detectors: Secondary electrons, Backscattered electrons , Auger electrons, and Characteristic X-rays , as illustrated in the figure: 4.5.
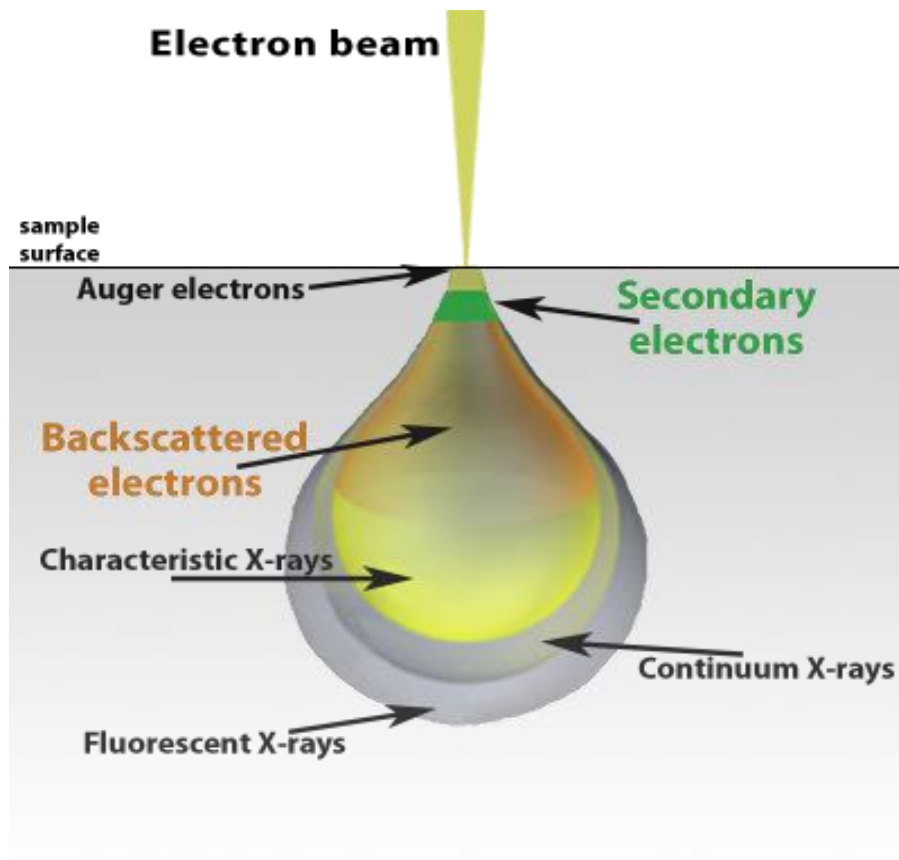
Figure 0.6: Types of Interactions at the Detector.

In our study, we used the SEM model SEM-JEOL-JSM-6490LA, which is equipped with a secondary electron detector and an energy dispersive spectroscopy (EDS) detector. This setup was utilized to examine surface topography and identify elemental distribution. The operating parameters were set with a voltage range of 10-20 kV and a working distance of 10 mm.

4.3 Fourier Transform Infrared Spectroscopy

This technique gathers data on absorption and emission spectra, Raman scattering, and photoconductivity. FTIR (Fourier Transform Infrared Spectroscopy) is used to determine the stretching modes of elements and the chemical purity of samples. The term "Fourier" refers to the mathematical transformation it uses. FTIR analyzes the light absorbed by a sample at specific wavelengths, collecting data across a spectrum.

Working of FTIR

In Fourier Transform Infrared (FTIR) spectroscopy, an infrared radiation beam is emitted by a polychromatic light source. This beam is then directed towards splitters. Half of the incoming light is deflected towards a fixed mirror , while the other half passes through a movable mirror. The light interacts with the sample medium, allowing for the collection of information regarding the molecular composition and structure of the sample.
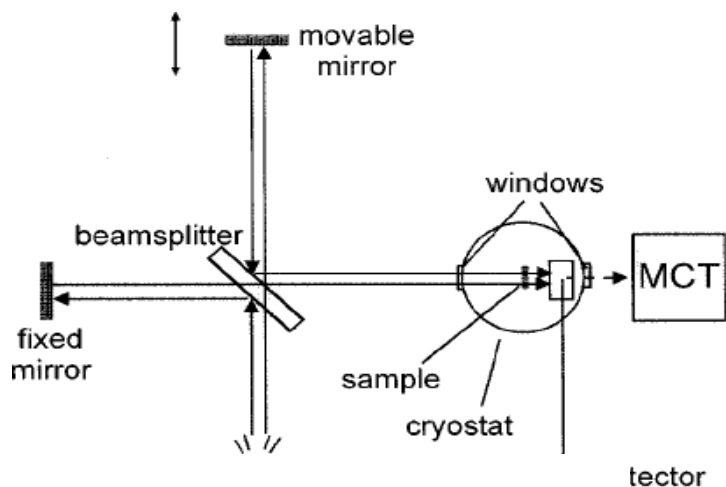
Figure 0.7: Schematics of FTIR.

Infrared rays occupy the space in the electromagnetic spectrum situated between the visible light and microwaves. They encompass wavelengths shorter than microwaves and longer than those of visible light. The infrared (IR) spectrum is categorized into three regions: far, mid, and near IR. The near IR pertains to the segment closest to visible light, while the far IR aligns more closely with the microwave region. The mid IR lies between these two extremes. Thermal radiation constitutes the primary source of infrared radiation, arising from the movement of molecules and atoms within a material. As temperature rises, more vigorous atomic motion leads to increased IR radiation emission.

In Fourier-transform infrared spectroscopy (FTIR), molecular vibrations occur because of absorption of IR radiation when the applied frequency matches the natural vibration frequency. Each bond or functional group within a molecule necessitates specific frequencies for absorption. Consequently, distinct peaks characteristic of each functional group or molecular segment are observed [73].

4.3.1   Application of FTIR

In both industry and research, FTIR method is widely utilized for quality control. It is a handy tool to utilize in field testing as well because it is a tiny and logistically efficient equipment.

Here are a few traits that define FTIR spectroscopy.

- Logistic efficient instrument for testing.
- Computer filters and result manipulation help to develop precise measurements.
- Wide range of reference spectrums can be stored to conveniently compare spectrum gained from material.
- Organic and inorganic materials can be examined.
- Efficient use in validation and identification of samples.
- Useful in the study of semiconducting materials.
- Valuable in measuring polymers' degree of polymerization.
- Helpful in finding variation in quality of specific bonds [74]

4.4   Electrochemical Profile Evaluation

Evaluating the supercapacitor's overall performance as well as its individual components is essential. Supercapacitor performance can be assessed by considering internal resistances, cyclic stability, power and energy densities, and capacitance. Every approach used to identify these components is electrochemical in nature. Electrochemical impedance spectroscopy (EIS), Galvanostatic charge-discharge (GCD), and cyclic voltammetry (CV) are common electrochemical tests used to assess supercapacitor performance.

Supercapacitor characterization involves two types of test configurations, 3 electrode and 2 electrode systems. The three-electrode system focuses on evaluating electrode materials using minimal quantities of active materials. In contrast, the two electrode configuration, which simulates a fully assembled supercapacitor, assesses the device's performance under conditions that approximate real-world usage.

4.4.1   Cyclic Voltammetry

Cyclic voltammetry (CV) assesses both quantitative and qualitative data related to the electrochemical processes occurring within the electrode materials of working electrodes. This technique provides valuable insights not only into the progression of electrochemical reactions but also into performance of supercapacitors, including capacitance and potential window, and long-term stability. CV is often used alongside galvanostatic charge-discharge (GCD) measurements as it offers complementary information and can be conducted using the same equipment.

During a CV test, an electrical potential is linearly varied between the electrodes in a two electrode setup, or between the reference and working electrodes in a three electrode setup. This potential moves back and forth between two predetermined values, limited by the electrolyte's stability. The rate at which the potential changes, measured in mVs^{-1}, is known as the scan rate or sweep rate, while the range of potential variation is referred to as the potential window. Instantaneous current during the cathodic and anodic scans is measured to analyze the electrochemical reactions. The data is typically recorded as current versus potential.

To compute electrode capacitance, active materials are applied to the surface of an inert electrode , which is then measured in electrolyte using CV. The resulting voltammogram of the electrode is used to calculate its capacitance.

GCD processes provide essential information of the electrochemical performance and efficacy of the entire supercapacitor device. They also reveal the device's dependence on consumption and environmental factors, such as temperature and state of charge etc.

4.4.2   Electrochemical Impedance Spectroscopy

Electrochemical impedance spectroscopy. (EIS), also referred to as dielectric spectroscopy or AC impedance spectroscopy, is widely utilized for analyzing the impedance data of supercapacitors. These tests involve subjecting the supercapacitor to an open-circuit voltage with a small voltage amplitude of ±5 or ±10 mV across a broad frequency range of 1 mHz to 1 MHz , lay over on a steady-state potential.

A typical Nyquist plot comprises three distinct sections. In the high-frequency region (greater than 10^4Hz), a semicircle usually manifests, representing the interface resistance attributed to the conductivity of the active materials and electrolyte. Moving from the high to medium frequency range (10^4Hz to 1Hz), the semicircle's diameter indicates the pseudo charge or charge transfer resistance, associated with the porous nature of the electrode. The low-frequency region (less than 1Hz) typically exhibits a nearly straight line along the imaginary axis, indicate the capacitive behavior[7]. In an ideal scenario, pure capacitors would display a line parallel to the imaginary axis , but deviations ranging from 45° to 90° to the real axis are observed in practice, reflecting ion diffusion mechanisms such as Warburg diffusion and pseudo-capacitive ion diffusion. These deviations can stem from redox reactions at the surface of electrode, leading to pseudo-capacitive behavior, or variations in AC signal penetration depth due to differences in electrode materials and pore size distributions.

EIS measurements serve multiple purposes, including the analysis of charge transfers, mass transportation, and charge storage Mechanisms , as well as the evaluation of device capacity, energy, and power density, frequency response and impedance. Various

equivalent circuits and models are employed to discern the influence of individual structural components within a device system on overall impedance. When assessing a supercapacitor device, the real part of the complex impedance at a designated frequency is utilized to indicate equivalent series resistance (RES). It's important to note that RES derived from Electrochemical impedance spectroscopy is typically much less than that calculated from GCD tests, hence inadequately describing the energy efficiency of supercapacitor devices[75].

4.4.3   Galvanostatic Charge Discharge

Galvanostatic Charge-Discharge test is the most widely used method for characterizing supercapacitors in DC current applications. This involves repeatedly charging and discharging the supercapacitor's cell or working electrode at a constant current , with or without a dwell time remains constant. The resulting data is potential versus time. Choosing an appropriate constant current value is crucial for obtaining reliable and comparable data from GCD tests. This test is considered the most versatile and accurate method for characterizing supercapacitor cells.

Using GCD, three parameters of supercapacitor capacitance, resistance, and peak potential can be tested and used to infer other important parameters such as time constant , power and energy density , leakage , and peak currents. This method is also useful for assessing the cyclic stability of supercapacitors. Additionally, using a three-electrode system allows for the evaluation of the active material's reversibility, capacitance, and potential window through GCD testing.

Cyclic voltammetry, Electrochemical impedance spectroscopy and galvanic charge discharge are done using "Gamry instrument" for which electrode setup is illustrated in figure 20 and 21.
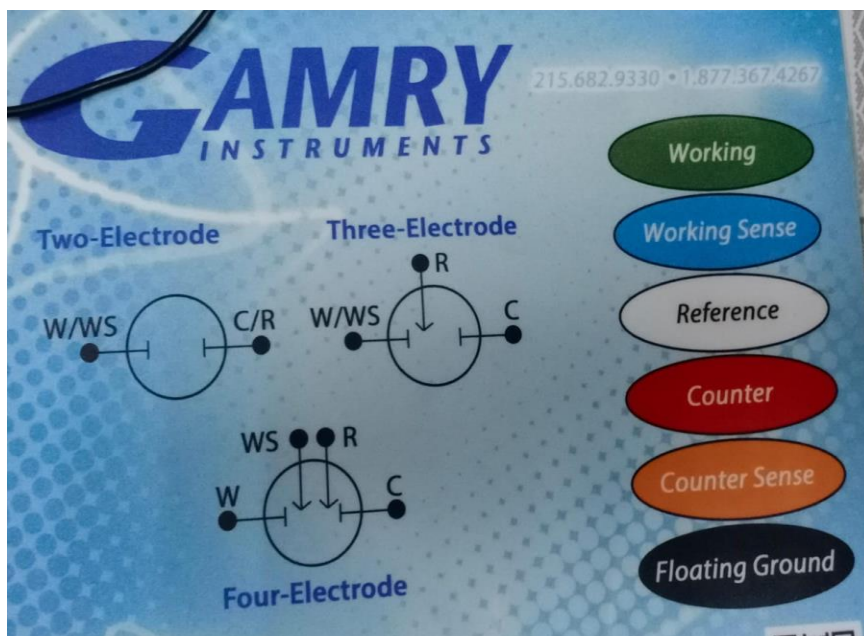
Figure 0.8: Electrode setup for Gamry Instrument

Figure 0.9: Electrode setup for CV.

CHAPTER 5: RESULTS AND DISCUSSION

This chapter is a continuation of the previous chapter (characterization techniques) and the results obtained from the characterization techniques are discussed here. The aim of the project is to synthesize an electrode material for supercapacitor application. For this purpose, four electrode materials are prepared ($ZnFe_2O_4$, $Zn_{0.5}Mg_{0.5}Fe_2O_4$, $Zn_{0.5}Co_{0.5}Fe_2O_4$ and $Zn_{0.5}Mg_{0.25}Co_{0.25}Fe_2O_4$) and their application testing was done (cyclic voltammetry, electrochemical impedance spectroscopy and galvanostatic charge discharge). Characterization techniques such as XRD, SEM and EDS are also discussed to support our results. Capacitance is calculated for all samples from both CV and GCD graphs. Resistance is calculated from EIS data and the Nyquist plots along with equivalent circuits are also drawn.

5.1   X-Ray Diffraction (XRD)

XRD analysis of all four samples is shown in Figure 5.1. The peaks at 29.98º, 35.3º, 36.9º, 56.7º and 62.3º corresponds to the (220), (311), (400), (440), (511), (333), (440), (400) planes respectively. The peaks at 35.3º and 62.3º is more intense, suggesting that the nanoparticles of all four samples are grown favorably along (311), (400) and (440) The peaks at the 2θ = 29.98º and 35.3º corresponded to the planes (220) and (311) are the characteristic peaks of pure $ZnFe_2O_4$ resembling with the typical pattern of $ZnFe_2O_4$ (ICDD card 01-086-0509, franklinite) as found in literature with Fd3m space group with cubic crystal structure. $Zn_{0.5}Mg_{0.5}Fe_2O_4$ resemble with (ICDD card 01-078-5430, magnesium zinc iron oxide). $Zn_{0.5}Co_{0.5}Fe_2O_4$ matches with (ICDD card 01-084-7431, cobalt zinc iron oxide) fcc-Fd3m. $Zn_{0.5}Mg_{0.25}Co_{0.25}Fe_2O_4$ showing resemblance to (ICDD card 01-083-4443, cobalt magnesium zinc iron oxide). Diffraction peaks of $ZnFe_2O_4$ and $Zn_{0.5}Co_{0.5}Fe_2O_4$ are also confirmed by the JCPDS card no: 22-1086, 89-1010, and 19-0629 found in literature [76].

The pattern for $ZnFe_2O_4$ shows well defined peaks indicating good crystalline cubic spinal structure in which Zn ions occupy tetrahedral sites and Fe ion occupy octahedral sites. Zn

and Fe influence the intensities of the peaks. Zn has higher atomic number thus it scatters X-rays more than Fe, affecting the peak intensities. Absence of any additional peaks represents purity of the $ZnFe_2O_4$.

Upon adding Mg into $ZnFe_2O_4$ the XRD pattern for $Zn_{0.5}Mg_{0.5}Fe_2O_4$ shows peaks and positions reflecting the specific distribution of Zn, Mg and Fe cations in the lattice. Peaks are slightly right shifted representing higher 2θ values indicating decrease in d-spacing value within crystal lattice. This happened when the larger cation Zn is substituted by a smaller cation Mg. Thus, the right shift can be attributed to successful doping of Mg.

The pattern for $Zn_{0.5}Co_{0.5}Fe_2O_4$ shows the spinal structure and the sharp peaks indicating good crystallinity. Absence of Mg peak in this pattern represents that the desired compound is formed. Slight shift towards right reflects the doping of cobalt and decrease in d spacing. The intensity of each diffraction peak depends on position and the type of the atom present in unit cell. Co ions sit at octahedral sites so the distribution of this compound on both octahedral and tetrahedral site causes change in peak position and lattice dynamics. Co and Fe have different atomic scattering compared to pure $ZnFe_2O_4$ where Zn has higher atomic number leading to change in peak intensity.

Similarly, $Zn_{0.5}Mg_{0.25}Co_{0.25}Fe_2O_4$ patterns show well defined diffraction peaks reflecting spinal crystal structure. The substitution of Co and Mg cause decrease in d spacing resulting shift in the peaks towards right. The symmetry in all peaks is due to doping.

The calculation of crystallite size and lattice constant is done using Scherrer equation and brag equation respectively [77]. The Scherrer equation is based on the width of the XRD peaks and expressed as:

$$D = \frac{K\lambda}{\beta cos\theta}$$

where D is the crystallite size, K is the Scherrer Constant , λ is the X-ray wavelength, β is the full width half maximum of the peak , and θ is the Bragg angle. Conversely, the Bragg equation allowed us to calculate the d-spacing of the XRD peaks, represented as:

$$d=\frac{\lambda}{sin\ 2\theta}$$

where d is the d-spacing, λ is the wavelength and θ is the Bragg angle [72]. Since the crystal structure is cubic, all four samples demonstrating Mg and Co are well doped into $ZnFe_2O_4$. The smaller crystallite size of $Zn_{0.5}Co_{0.5}Fe_2O_4$ indicates large surface to volume ratio and consequently, providing more active sites for electrochemical reaction and improves materials ability to store charges. This also indicates less internal resistance which overall improves material's conductivity and better utilization of the material.
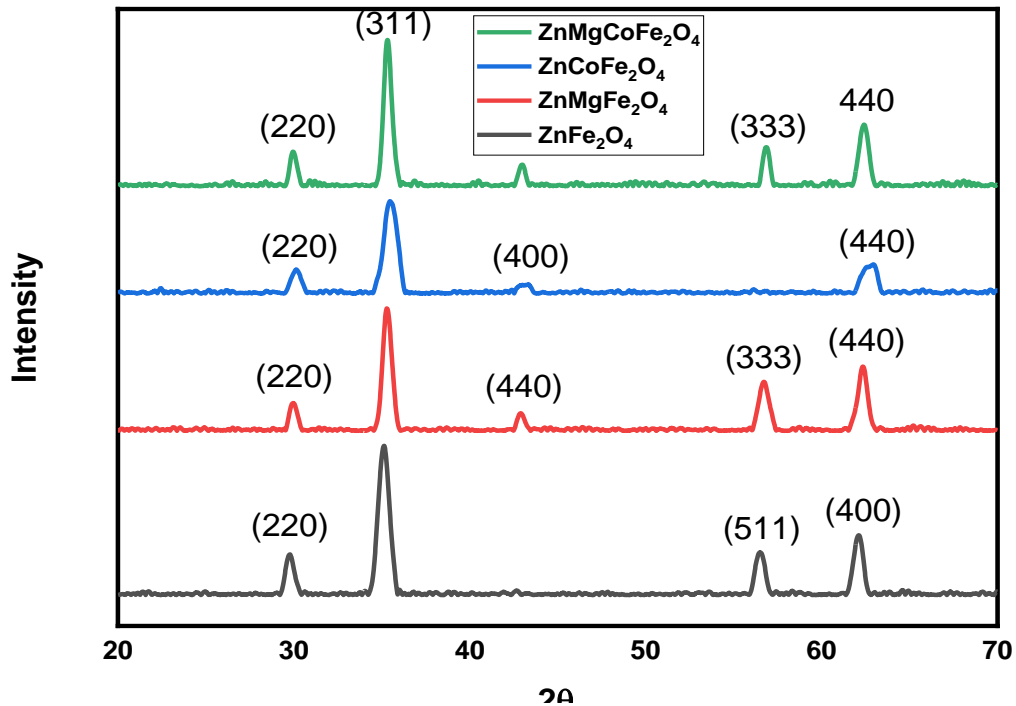
Figure 0.10: XRD diffraction pattern of $ZnFe_2O_4$, $Zn_{0.5}Mg_{0.5}Fe_2O_4$, $Zn_{0.5}Co_{0.5}Fe_2O_4$ and $Zn_{0.5}Mg_{0.25}Co_{0.25}Fe_2O_4$

Table 0.1: Crystallite Size and Lattice Constant of $ZnFe_2O_4$, $Zn_{0.5}Mg_{0.5}Fe_2O_4$, $Zn_{0.5}Co_{0.5}Fe_2O_4$, and $Zn_{0.5}Mg_{0.25}Co_{0.25}Fe_2O_4$

Samples	Crystallite Size (nm)	Crystal Structure (FCC)	Lattice Constant (Å)
$ZnFe_2O_4$	15	Cubic	8.426
$Zn_{0.5}Mg_{0.5}Fe_2O_4$	17	Cubic	8.420
$Zn_{0.5}Co_{0.5}Fe_2O_4$	10	Cubic	8.409
$Zn_{0.5}Mg_{0.25}Co_{0.25}Fe_2O_4$	18	Cubic	8.390

5.2 Scanning Electron Microscopy (SEM):

A suspension of synthesized material is dropped on a glass substrate for morphological study. This process is essential for observing the structure and characteristics of the material at microscopic level. Scanning electron microscopy is a powerful technique that provides high resolution images of sample's surface to observe shape size and distribution of the particles. Figure 5.2 shows the morphology and size of particles of $ZnFe_2O_4$, $Zn_{0.5}Mg_{0.5}Fe_2O_4$, $Zn_{0.5}Co_{0.5}Fe_2O_4$ and $Zn_{0.5}Mg_{0.25}Co_{0.25}Fe_2O_4$.

Image (a) in Figure 5.2 for $ZnFe_2O_4$ shows agglomeration of the particle of irregular size. This morphology and clustering indicate the presence of relatively large particles. The agglomeration is due to the magnetic interaction between the particles [78, 79]. Agglomeration reduces the effective area for electrochemical reaction, limiting the contact between electrolyte and the active material resulting in reduced capacitance. Moreover, the

larger crystallite size may cause reduction in the number of grain boundaries limiting electrochemical active sites available for ion intercalation and de-intercalation process. Dense cluster can also affect ion diffusion, slowing down charge discharge process.

Image (b) in Figure 5.2 indicates that the particles of $Zn_{0.5}Mg_{0.5}Fe_2O_4$ are in cluster form but the agglomeration is relatively less. Mg appears to provide more uniform morphology and particle distribution. Smaller size of Mg helps in reducing crystallite growth but not enough reduce to be favorable for electrochemical reduction. The agglomeration leads to poor electrical conductivity resulting in poor performance of supercapacitors. Agglomeration tends to mechanical instability during charge discharge cycle resulting in material degradation and cyclic stability.

SEM of $Zn_{0.5}Co_{0.5}Fe_2O_4$ in Figure 5.2 (c) shows less agglomeration and appears to be smoother. The substitution of Co leads to uniformly distributed particles of smaller crystallite sizes. The small crystallite size refers to the large surface area resulting in more grain boundaries which provide more active sites favorable for redox reaction. The smooth surface indicates distinct particles which further enhance the surface area resulting in efficient electrolyte interaction leading to higher capacitance. Less agglomeration facilitates ion diffusion hence improving the rate capability and efficiency of supercapacitor. These small well distributed particles contribute in the maintenance of mechanical stability during charging and discharging.

Figure 5.2 (d) for $Zn_{0.5}Mg_{0.25}Co_{0.25}Fe_2O_4$ appears to be a mixture of agglomerated and well define particles. Agglomeration negates the benefit of enhanced surface area for ions and active material interactions resulting in poor capacitance. Dense cluster hindered the diffusion process resulting in low conductivity. SEM images indicate the favorable morphology of $Zn_{0.5}Co_{0.5}Fe_2O_4$ for supercapacitor application because of its high diffusional properties, high surface area and better mechanical stability.

All of the photos have the same 50,000x magnification with 0.5 micrometer scale bar. The accelerating voltage was 20 kV. SEM provides an estimate of the size, shape, and surface morphology of ferrite nanoparticles.
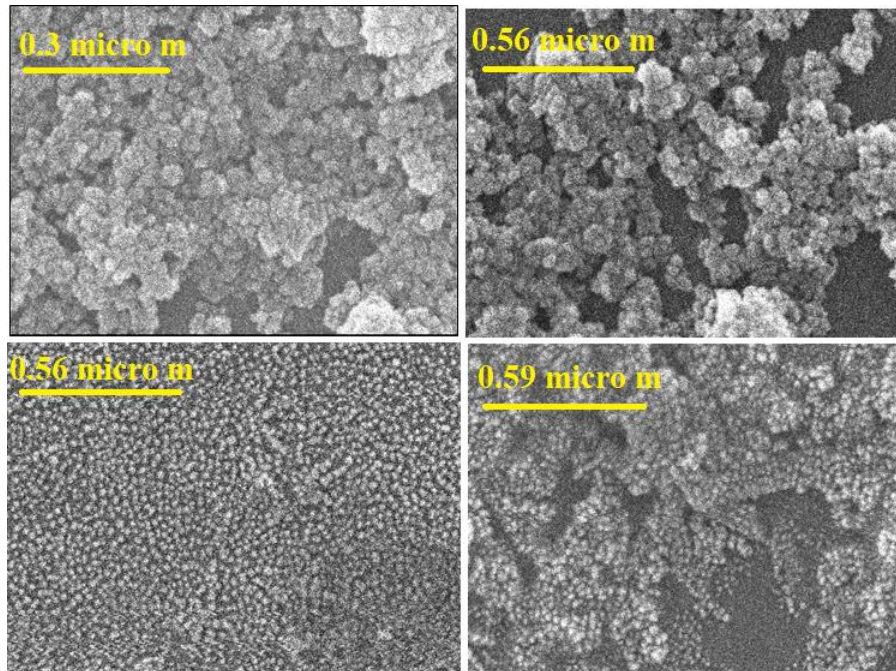
Figure 0.11 SEM images of $ZnFe_2O_4ZnFe_2O_4$, $Zn_{0.5}Mg_{0.5}Fe_2O_4$, $Zn_{0.5}Co_{0.5}Fe_2O_4$ and $Zn_{0.5}Mg_{0.255}Co_{0.25}Fe_2O_4$

Table 0.2: Average particle Size

Sample	Average Particle Size nm
$ZnFe_2O_4$	55
$Zn_{0.5}Mg_{0.5}Fe_2O_4$	68.1
$Zn_{0.5}Co_{0.5}Fe_2O_4$	33.1
$Zn_{0.5}Mg_{0.25}Co_{0.25}Fe_2O_4$	143

5.3   Energy Dispersive X-Ray (EDX)

EDX technology is used to analyze the sample in order to determine their elemental composition. There is no need for any separate setup for EDX, it is often used in conjunction with scanning electron microscopy providing a comprehensive understanding of the elemental makeup of the sample. This integration makes it a potent tool in materials research by enabling simultaneous morphological and compositional investigation. For all samples prepared, Iron, Zinc, cobalt, and magnesium contents are verified as illustrated in Figure 5.3. Peak intensity confirms the concentration of O, Fe and Zn for sample $ZnFe_2O_4$ along with distinct peaks of these elements. The Kα and Kβ lines of iron (Fe) correlate to significant peaks in the spectrum appearing at 6.4 keV and around 7.1 keV, respectively, suggesting that iron is the main element in the sample. Similarly, Mg peak can be seen for $Zn_{0.5}Mg_{0.5}Fe_2O_4$ along with Zn, iron, and oxygen. This confirms the incorporation of magnesium in $ZnFe_2O_4$. Similarly Cobalt peaks confirm its presence for sample $Zn_{0.5}Co_{0.5}Fe_2O_4$. Magnesium and cobalt both can be seen in Figure 5.3 (d) for the sample $Zn_{0.5}Mg_{0.25}Co_{0.25}Fe_2O_4$.

Table: 5.3 provides specific weight and atomic percentage values of $ZnFe_2O_4$, $Zn_{0.5}Mg_{0.5}Fe_2O_4$, $Zn_{0.5}Co_{0.5}Fe_2O_4$ and $Zn_{0.5}Mg_{0.25}Co_{0.25}Fe_2O_4$ suggesting that samples do not have any impurity. Unidentified peaks are the peaks of gold as gold coating is done while the samples are subjected to Scanning electron microscopy. The effective completion of the synthesis process and the achievement of the intended stoichiometry are guaranteed by the accurate quantification of every element in the samples. Table 5.3 has confirmed the atomic weight percentage of the element according to their respective ratios. The quality and purity are further confirmed by the lack of unanticipated components, which qualifies them for possible use in a variety of industries including energy storage, magnetic materials, and catalysis.
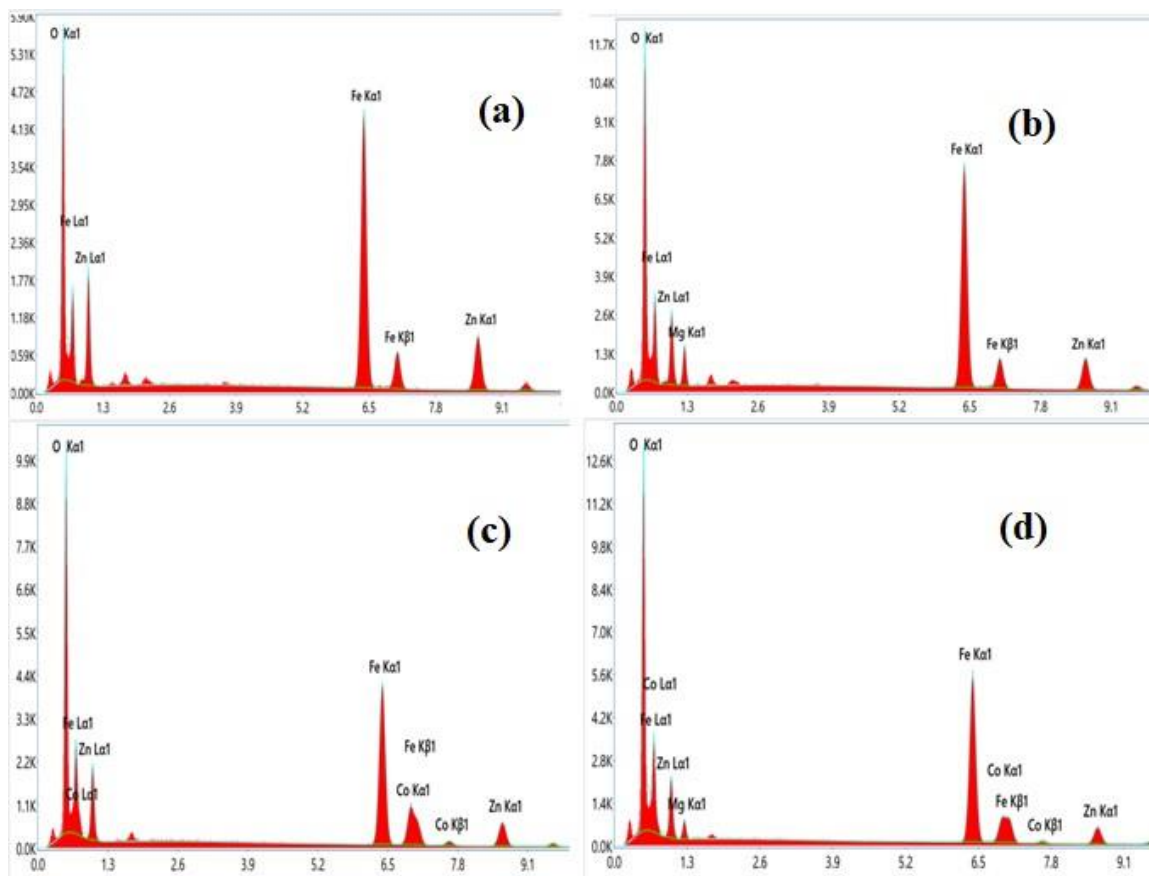
Figure 0.12: EDX of (a) $ZnFe_2O_4$, (b) $Zn_{0.5}Mg_{0.5}Fe_2O_4$, (c) $Zn_{0.5}Co_{0.5}Fe_2O_4$ and (d) $Zn_{0.5}Mg_{0.25}Co_{0.25}Fe_2O_4$

Table 0.3: Weight and Atomic Percentage of Elements

$ZnFe_2O_4$		
Element	Weight %	Atomic %
O	24.7	54.5
Fe	52	32.9
Zn	23.3	12.6

$ZnMgFe_2O_4$		
Element	Weight %	Atomic %
O	27.7	55.8
Mg	5.1	6.8
Fe	50.8	29.3
Zn	16.4	8.1

$ZnCoFe_2O_4$		
Element	Weight %	Atomic %
O	32.8	63.9
Fe	41.8	23.4
Co	11.1	5.9
Zn	14.3	6.8

$ZnMgCoFe_2O_4$		
Element	Weight %	Atomic %
O K	33.6	63.3
Mg K	2.8	3.5
Fe K	45.4	24.5
Co K	7.6	3.9
Zn K	10.6	4.9

5.4   Fourier Transform Infrared Spectroscopy (FTIR)

In order to clarify the chemical makeup of synthesized materials, we performed Fourier-transform infrared (FTIR) spectroscopy analysis on four samples. Using this method, we measure the adsorption of infrared radiation at different wavelengths and determine different functional groups and bonds that are present in the compounds.

FTIR for $ZnFe_2O_4$ shows an absorption band attributed to M-O stretching vibration in 560 cm^{-1} region. This high frequency band represents tetrahedral sites. Other M-O stretching at 353 cm^{-1} is low frequency region representing octahedral sites. Since there is no dopant so the peak is well defined. Pure $ZnFe_2O_4$ provides a stable platform for electrochemical reactions but may have less conductivity as compared to doped version.

$Zn_{0.5}Mg_{0.5}Fe_2O_4$ shows spinal structure of ferrite along with the peaks around 570- cm^{-1} (higher wavenumber) representing tetrahedral sites and M-O bonding. Peaks at 407 cm^{-1} and 393 cm^{-1} showing M-O bond vibrations at octahedral sites. The peaks are slightly shifted to the right indicating Mg has been successfully incorporated in $ZnFe_2O_4$. Substitution of Mg lead to smaller particle size and high surface area but the SEM images show the clustering and agglomeration of the particles leading to decrease in overall surface area.

FTIR spectrum of $Zn_{0.5}Co_{0.5}Fe_2O_4$ show absorption band around higher wavenumber at 576 cm^{-1} representing tetrahedral sites and M-O bonding. Peaks at lower wavenumber of 385, 362, 356 cm^{-1} representing M-O bond vibration at octahedral sites. The spectrum is consistent with spinal ferrite structure interpreting the successful incorporation of Co into

the lattice. Both Zn and Co are in tetrahedral sites, so the peaks are slightly shifted. Inclusion of Co increases electrical conductivity and magnetic properties, hence providing redox sites, enhancing energy storage capacity and capacitance. Metal oxygen bond provide structural stability and ensure better electrochemical performance.

$Zn_{0.5}Mg_{0.25}Co_{0.25}Fe_2O_4$ also exhibits the spinal structure and characteristic peaks of ferrites
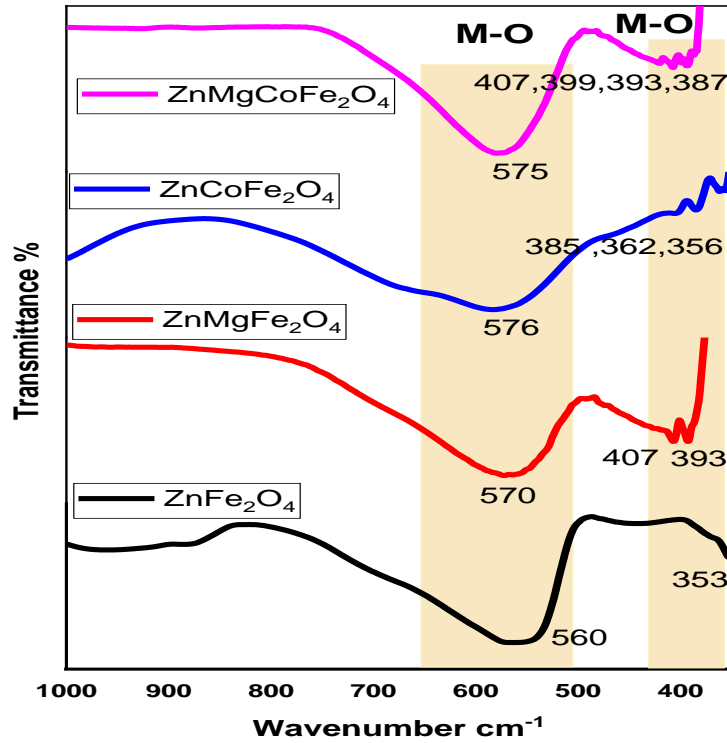
indicating M-O bonding. Peak at higher wavenumber of 575 cm^{-1} represent tetrahedral sites. Peaks at 407, 399, 393 and 387 cm^{-1} represent octahedral sites. Mg and Co is present in the structure as the peaks are right shifted. The presence of Zn, Mg and Co make a complex structure causing variation in peak position. This combination can increase particle size and surface area, but agglomeration decreases overall surface area.

Figure 0.13: FTIR spectra of $ZnFe_2O_4$, $Zn_{0.5}Mg_{0.5}Fe_2O_4$, $Zn_{0.5}Co_{0.5}Fe_2O_4$ and $Zn_{0.5}Mg_{0.25}Co_{0.25}Fe_2O_4$

5.5   Cyclic Voltammetry

Cyclic   voltammetry   of $ZnFe_2O_4$, $Zn_{0.5}Mg_{0.5}Fe_2O_4$, $Zn_{0.5}Co_{0.5}Fe_2O_4$ and
$Zn_{0.5}Mg_{0.25}Co_{0.25}Fe_2O_4$ on nickel foam at different scan rates of 5 mVs^{-1}, 10 mVs^{-1}, 20
mVs^{-1} 50 mVs^{-1}, 100 mVs^{-1} and 200 mVs^{-1}shown in Figure 5.5.
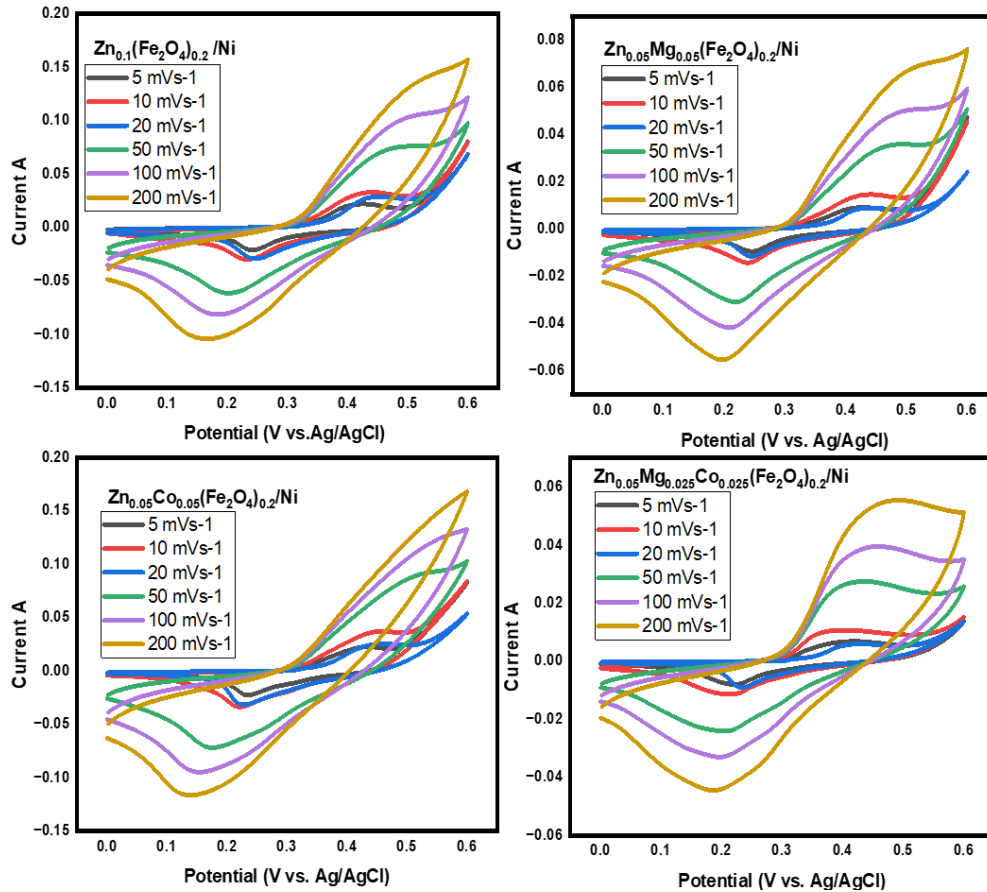
Figure 0.14: Cyclic Voltammetry

Comparative studies of cyclic voltammetry of all four samples at 5mVs^{-1} show a definite
Faradic peak within a potential window of 0 to 0.6mV shown in Figure 34. This window
could be attributed to reversible redox reaction of Zn, Mg, Co [81-83]. The symmetric and
nearly rectangular curve indicate almost pseudocapacitive behavior with fast ionic
intercalation on electrode surface. Specific capacitance of electrode material using CV
curves are found by the formula given below:

$$C_s = \frac{\int I \, dV}{2mV_s\Delta V}$$

Where "∫" is the integral area under the CV curve , "m" is the active mass of electrode material ,

"Vs" is the scan rate and "ΔV" is the potential window. Results show improved capacitance of , $Zn_{0.5}Co_{0.5}Fe_2O_4$ as compared to its counterparts as represented in Table 5.4. Zn and Co doping change the ferrite's microstructure and produce grain boundaries that are clearly defined. These grain boundaries serve as areas where charges build up, raising the capacitance and overall dielectric constant. Cation distribution between the tetrahedral (A) and octahedral (B) sites can change when Zn and Co ions are substituted in the ferrite lattice. This increases the material's capacity to hold electric charge by altering the ionic polarizability. Hence this doping exhibit enhanced capacitance.

Table 0.4: Specific Capacitance values.

Sample	Specific Capacitance F/g	Internal resistance (ohm)
$ZnFe_2O_4$	306.584	1.6
$Zn_{0.5}Mg_{0.5}Fe_2O_4$	201.058	1.45
$Zn_{0.5}Co_{0.5}Fe_2O_4$	325.670	1.154
$Zn_{0.5}Mg_{0.25}Co_{0.25}Fe_2O_4$	94.527	1.596

From the graphs, it can be observed that the integral area of $Zn_{0.5}Co_{0.5}Fe_2O_4$ is greater than its counterparts which directly influence the charge storage and release during

electrochemical cyclic process. It can also be observed by the aforementioned equation that area is related to the capacitance of the electrode. The more the area, the more charges will be stored which results in higher capacitance, charge storage. It is observed that by increasing the scan rate, peak current also increases, which indicates that the scan rate is directly proportional to current density. CV profiles formed without any deformation, representing that pseudocapacitive charge storage features by rapid charge transport and storage capacity [84].

Specific capacitance of Magnesium doped ferrites does not show high or improved capacitance due to many reasons including atomic radii, electronic configuration, polarizability, grain size, magnetic properties, defects, and microstructural characteristic induced by doping element. Magnesium has smaller radii resulting more compact and less distorted lattice structure with the electronic configuration of $1s^2 2s^2 2p^6$ which cause reduction in polarization and less responsive to external electric fields. The induction of magnesium in zinc leads to the formation of defects that reduce mobility of charges thus reducing capacitance.

Due to the non-magnetic nature of Mg^{+2} ions, it can change the magnetic interactions in the ferrite matrix, effecting dielectric characteristics and reducing capacitance. Although zinc ions are likewise non-magnetic, their impact on magnetic and dielectric coupling in ferrites tends to strengthen the dielectric qualities and consequently increase capacitance.

Figure 5.6 represents the comparative CV results at $5mVs^{-1}$. At lower scan rate, there is more time for ions diffusion which gives a large integral area and hence greater capacitance and energy density. $Zn_{0.5}Co_{0.5}Fe_2O_4$ shows a large integral area and hence greater capacitance as mentioned in Table 5.4.

Peak position and the shift in peak position represent redox potential and change in redox behavior. Figure 5.6 represents decent redox activity along with moderate potential window, reasonable capacitance and energy storage for $ZnFe_2O_4$. $Zn_{0.5}Mg_{0.5}Fe_2O_4$ shows a narrow window indicating low energy storage capacity. The shift may be caused by Mg which affects the redox potential and overall performance compared to $ZnFe_2O_4$. $Zn_{0.5}Co_{0.5}Fe_2O_4$ is showing a wider window indicating high energy storage capacity, likely

to improve capacitance. $Zn_{0.5}Mg_{0.25}Co_{0.25}Fe_2O_4$ shows broad peak with less integral area indicating low kinetics and diffusion.
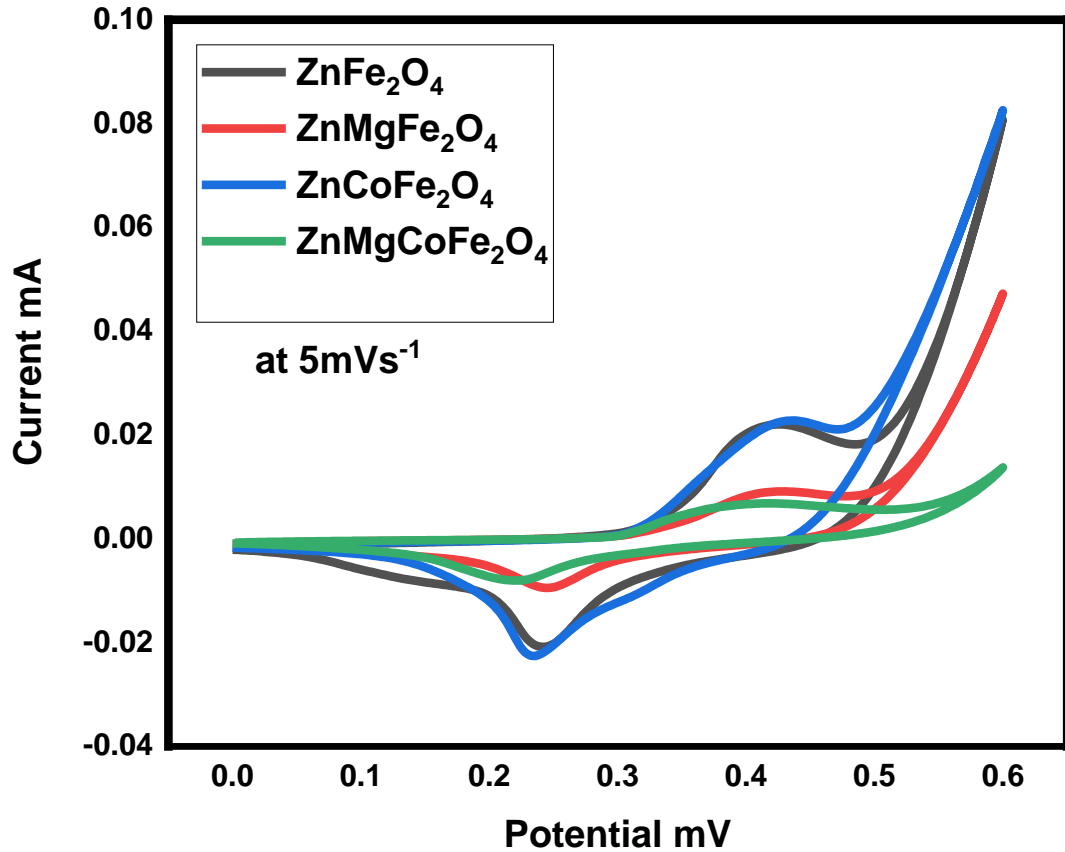
Figure 0.15: Comparison of Cyclic Voltammetry curves at 5 mVs-1

5.6   Electrochemical Impedance Spectroscopy (EIS)

Studying the EIS analysis is an approach, to investigate the characteristics of electrode materials, for supercapacitors. EIS involves subjecting the supercapacitor material to an open-circuit voltage across a broad frequency range of 0.1 Hz to 100 mHz over a steady state potential. EIS provides a valuable insight into resistive and capacitive properties of the material. Nyquist plots of all electrodes showed a similar pattern, which is a common feature in the analysis of supercapacitor materials. These plots consist of two distinct

regions, a semi-circle at high frequency region and a straight line is lower frequency region. The semi-circle in the high frequency region represents the resistance of the materials. The charge transfer resistance (RCT) can be directly measured by measuring the semi-circle's diameter. A lower RCT, which is indicated by a smaller diameter, implies that the electrode material has effective charge transfer properties and strong electrochemical reactivity. The series resistance (Rst) is represented by the intercept on the real axis (Z') at the start of the semicircle. A lower intercept value indicates a lower systemic resistance, which is essential for supercapacitors to achieve high power densities.

The electrochemical reaction that takes place at the contact between electrode and electrolyte are linked to its resistance. RCT specifically measures the difficulty of transferring electrons from the electrode material to ions in the electrolyte and vice versa. Smaller RCT value indicates efficient charge transfer is desirable for high performance supercapacitors. Lower RCT represents that the electrode material can facilitate faster and efficient redox reaction which helps in faster charging and discharging cycles. RCT value is influenced by several factors such as intrinsic electrical conductivity of the electrode material, the surface area available for reactions, the quality of contact between electrode and electrolyte etc.

Series resistance (Rst) is also known as solution resistance or ohmic resistance. The ionic resistance of the electrolyte, the electronic resistance of the electrode material, and the contact resistance between the electrode and the current collector all contribute to this resistance. Overall better conductivity is achieved via a lower Rst value, which denotes less resistance to the movement of ions and electrons within the system. Lowering Rst contributes to less energy loss and increased supercapacitor efficiency. The value of Rst can be affected by the conductivity of the electrolyte, the porosity and structure of the electrode material, and the quality of the contacts within the electrochemical cell. Evaluation of the electrode material's effectiveness in terms of both electron and ion transport can be done by examining the high-frequency portion of the Nyquist plot. With the help of this data, supercapacitors' performance and design may be optimized to satisfy the demands of a wide range of applications. The straight line indicates the electrodes

blocking behavior. The sharp spike signifies the movement of ions, in the solution and their swift adsorption on the electrodes surface[84].

The internal resistance obtained from the software "ZsimWin" is 1.6 ohm, 1.45 ohm, 1.154 ohm and 1.596 ohm respectively and measured and fitted Nyquist plot for along with its equivalent circuit is shown in Figure 5.7. This resistance can be corelate to the XRD, SEM, EDX, FTIR, and CV results discussion. $Zn_{0.5}Co_{0.5}Fe_2O_4$ shows high capacitance so it has low resistance.
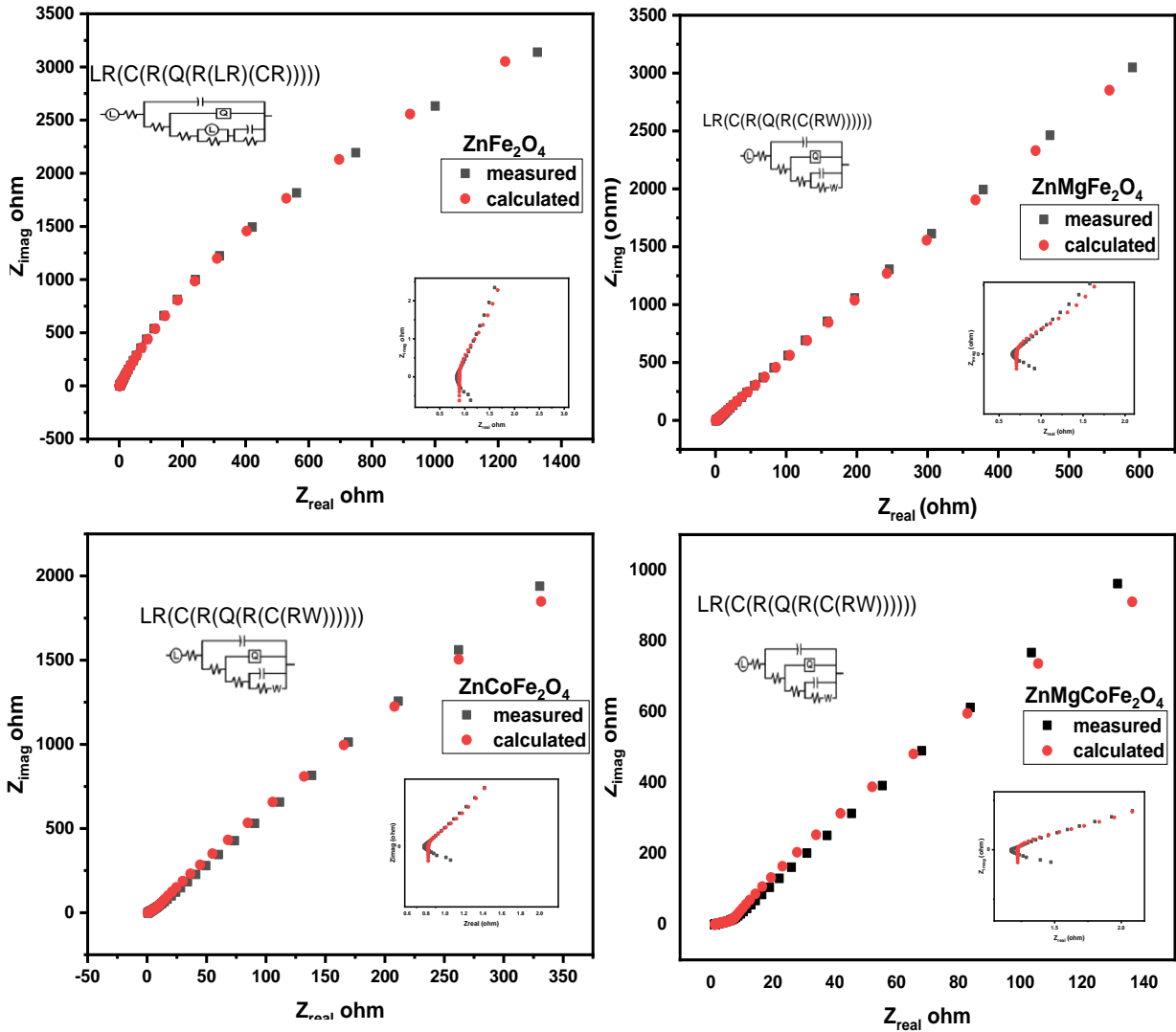

Figure 0.16: Nyquist Plot of $ZnFe_2O_4$, $Zn_{0.5}Mg_{0.5}Fe_2O_4$, $Zn_{0.5}Co_{0.5}Fe_2O_4$ and $Zn_{0.5}Mg_{0.25}Co_{0.25}Fe_2O_4$

5.7 Galvanic Charge Discharge (GCD)

A comparative analysis of GCD for four electrodes is shown in Figure 5.8. This analysis validates the rate capabilities at 0.5 A/g. GCD curves offer crucial information about the effectiveness and performance of the electrode material in supercapacitors. The initial vertical drop at the start of the discharge curve indicates internal resistance (IR) of the electrode material. $ZnFe_2O_4$ shows moderate IR drop indicating low internal resistance. Its discharge time is 302 seconds. $Zn_{0.5}Mg_{0.5}Fe_2O_4$ also shows less resistance from IR drop. Its discharge time is also very low (352 seconds), so it is less favorable for high performance supercapacitors. $Zn_{0.5}Mg_{0.25}Co_{0.25}Fe_2O_4$ shows discharge time of 250 seconds with low IR drop indicating low internal resistance. Among the four electrode $Zn_{0.5}Co_{0.5}Fe_2O_4$ exhibits a significantly longer discharge time of 530 seconds with minimal internal resistance. This indicates higher energy storage capacity compared to other electrodes. Discharge time reflects the varying capacities of each electrode material to store and release energy. Throughout the process of charging and discharging the GCD curves displayed a higher degree of symmetry. This symmetry is a desired quality since it shows that the electrode materials are stable and perform consistently. The symmetrical GCD curves are also well aligned with cyclic voltammetry profiles confirming the repeatability and reliability of the electrochemical behavior. Higher discharge period than the charging period indicates that the $Zn_{0.5}Co_{0.5}Fe_2O_4$ electrode has a high Coulombic efficiency. The effectiveness with which the charge accumulated during the charging phase may be recovered during the discharging process is measured by the Coulombic efficiency. A system with a high Coulombic efficiency has little energy loss and efficient charge transfer. $Zn_{0.5}Co_{0.5}Fe_2O_4$ has superior Coulombic efficiency, which can be attributed to favorable electrochemical interactions between the electrolyte and electrode material. The four electrode materials function differently, as shown by the comparative analysis of GCD curves; $Zn_{0.5}Co_{0.5}Fe_2O_4$ exhibits the most promising findings in terms of discharge time and energy storage capacity. These results offer important insights into the efficiency and rate capabilities of various electrode materials, which are critical for the design and development of high-performance-supercapacitors. The specific capacitance corresponding to the current density of 0.5 A/g is calculated using the expression below:

$$Cs= \frac{I*\Delta t}{\Delta V}$$

The ZnFe$_2$O$_4$ shows moderate capacitance because of low redox activity, Zn$_{0.5}$Mg$_{0.5}$Fe$_2$O$_4$ reasonable capacitance but due to agglomeration and less surface area the electrochemical activity is less. Zn$_{0.5}$Co$_{0.5}$Fe$_2$O$_4$ shows high capacitance indicating enhanced redox activity and Zn$_{0.5}$Mg$_{0.25}$Co$_{0.25}$Fe$_2$O$_4$ shows lowest capacitance.
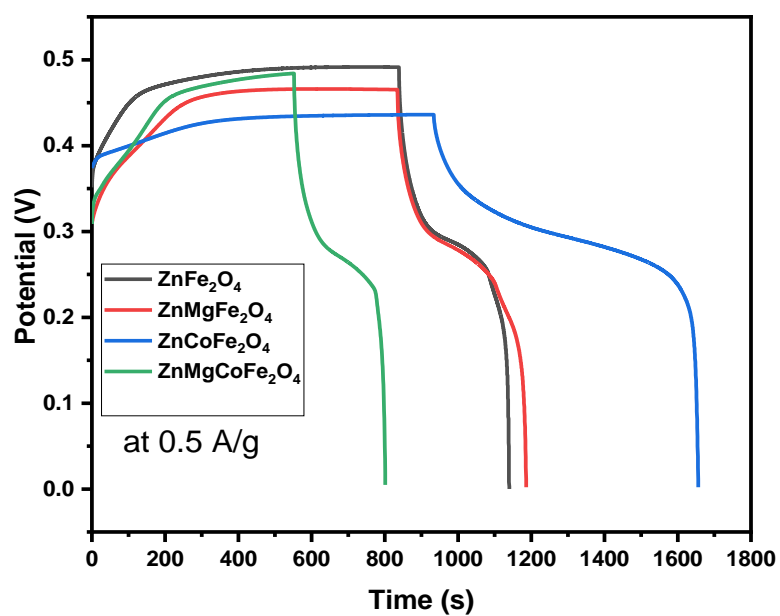

Figure 0.17: GCD at 0.5 A/g

Table 5.5: Specific Capacitance using GCD Plots.

Sample	Current (A/g)	Specific Capacitance
$ZnFe_2O_4$	0.5	380.13
$Zn_{0.5}Mg_{0.5}Fe_2O_4$	0.5	309.57
$Zn_{0.5}Co_{0.5}Fe_2O_4$	0.5	530.00
$Zn_{0.5}Mg_{0.25}Co_{0.25}Fe_2O_4$	0.5	260.96

CHAPTER 6: CONCLUSIONS AND FUTURE RECOMMENDATION

6.1 Conclusion

In summary, $ZnFe_2O_4$, $Zn_{0.5}Mg_{0.5}Fe_2O_4$ $Zn_{0.5}Co_{0.5}Fe_2O_4$ and $Zn_{0.5}Mg_{0.25}Co_{0.25}Fe_2O_4$ were successfully prepared by coprecipitation method, and their properties were studied using analytical techniques like XRD, SEM, and EDX. Electrochemical properties were studied via cyclic voltammetry , electrochemical impedance spectroscopy and galvanic charge discharge. This work has opened the door to advancements in energy storage, especially with the doping of cobalt and zinc ferrite. This electrode material has potential to be used in energy storage devices especially in supercapacitors and it has been made clear by their thorough characterizations. XRD results show well defined peaks indicating good crystalline cubic spinal structure in which Zn ions occupy tetrahedral sites and Fe ion occupy octahedral sites and with the doping of Mg and Co the peaks are slightly right shifted. This happens because with this inclusion d-spacing (Braggs law) decreases and 2θ increases. SEM images show agglomeration for $ZnFe_2O_4$, $Zn_{0.5}Mg_{0.5}Fe_2O_4$ and $Zn_{0.5}Mg_{0.25}Co_{0.25}Fe_2O_4$ which cause clustering resulting in less redox active sites and low diffusion of ion and hence provide less capacitance whereas, $Zn_{0.5}Co_{0.5}Fe_2O_4$ shows uniform distribution of particles providing more active sites, large surface area resulting in high capacitance values. EDX results confirm the presence of elements in synthesized samples and validate the atomic percentage of the elements. FTIR show the absorbance and bond vibrating (M-O) and their role in facilitating electrochemical reaction. CV provides an insight of integral area and capacitance for all four electrode materials. The more the area the more will be the active sites and charge storage capacity of the electrode. With the doping of Mg, the specific capacitance decreases. This might be due to unavailability of any unpair electron. Moreover, Mg substitute Fe in octahedral site, disrupting pathway for electron hoping which leads to lower electrical conductivity. Stronger M-O bond restrict the ion moment in lattice structure. Out of all $Zn_{0.5}Co_{0.5}Fe_2O_4$ shows high specific capacitance of 325.670 F/g and low resistance of 1.15 ohm obtained by EIS. GCD results has also shown capacitance of 530 F/g with a discharge time of 530

72

sec at 0.5 A/g. Internal resistance (IR) drop of the electrode material also show minimum resistance for $Zn_{0.5}Co_{0.5}Fe_2O_4$. This is because of unpair d electron of Co. Co can occupy both tetrahedral and octahedral sites leading to flexible lattice structure that enhances ion mobility. Co and Fe participate in electron hoping, enhancing electronic conductivity and hence capacitance. In $Zn_{0.5}Mg_{0.25}Co_{0.25}Fe_2O_4$ Mg tend to stabilize the spinal structure by occupying tetrahedral and octahedral sites, but the stability come at the cost of reduced electronic conductivity and ionic mobility. Co enhanced conductivity diminished by Mg. The reduced formation of oxygen vacancies in the presence of Mg^{2+} leads to fewer active sites for redox reactions and less structural flexibility, contributing to the overall decline in capacitance. Therefore, Zn and Co doped ferrites contribute to improved capacitance Their high capacitance makes them desirable for use in capacitors and other electronic components.

6.2 Future recommendation

Doping with other transition metals can be explored for studying their electrochemical properties. Development of hybrid composite of $Zn_{0.5}Co_{0.5}Fe_2O_4$ with MXene, graphene and carbon nanotubes for improved electrochemical properties.

REFERENCES

[1]   C. D. J. F. a. Igwebike-Ossi and prevention, "X-ray techniques," vol. 10, 2017.

[2]   B. K. Kim, S. Sy, A. Yu, and J. J. H. o. c. e. s. Zhang, "Electrochemical supercapacitors for energy storage and conversion," pp. 1-25, 2015.

[3]   M. Bohra, V. Alman, and R. Arras, "Nanostructured ZnFe2O4: An Exotic Energy Material. Nanomaterials 2021, 11, 1286," ed: s Note: MDPI stays neu-tral with regard to jurisdictional claims in …, 2021.

[4]   H. Chen, L. Zhao, W. Fang, W. Li, X. He, and F. J. J. o. M. S. M. i. E. Zhang, "Construction of hierarchical NiCo 2 S 4 nanowires on 3D biomass carbon for high-performance supercapacitors," vol. 29, pp. 9573-9581, 2018.

[5]   S. Jung, Y. Myung, B. N. Kim, I. G. Kim, I.-K. You, and T. J. S. r. Kim, "Activated biomass-derived graphene-based carbons for supercapacitors with high energy and power density," vol. 8, no. 1, p. 1915, 2018.

[6]   Y. Li *et al.*, "A NiCo2S4/hierarchical porous carbon for high performance asymmetrical supercapacitor," vol. 427, pp. 138-144, 2019.

[7]   M. M. Baig, I. H. Gul, M. Z. Khan, M. T. Mehran, and M. S. J. E. A. Akhtar, "Binder-free heterostructured MWCNTs/Al2S3 decorated on NiCo foam as highly reversible cathode material for high-performance supercapacitors," vol. 340, p. 135955, 2020.

[8]   R. Ahmad, N. Iqbal, M. M. Baig, T. Noor, G. Ali, and I. H. J. E. A. Gul, "ZIF-67 derived nitrogen doped CNTs decorated with sulfur and Ni (OH) 2 as potential electrode material for high-performance supercapacitors," vol. 364, p. 137147, 2020.

[9]   Elizbit, U. Liaqat, Z. Hussain, M. M. Baig, M. A. Khan, and D. J. J. o. t. K. C. S. Arif, "Preparation of porous ZIF-67 network interconnected by MWCNTs and decorated with Ag nanoparticles for improved non-enzymatic electrochemical glucose sensing," vol. 58, no. 5, pp. 598-605, 2021.

[10]   M. M. Baig, I. H. Gul, R. Ahmad, S. M. Baig, M. Z. Khan, and N. J. J. o. M. S. Iqbal, "One-step sonochemical synthesis of NiMn-LDH for supercapacitors and overall water splitting," vol. 56, pp. 18636-18649, 2021.

[11]   B. Anasori, M. R. Lukatskaya, and Y. J. N. R. M. Gogotsi, "2D metal carbides and nitrides (MXenes) for energy storage," vol. 2, no. 2, pp. 1-17, 2017.

[12]   M. M. Baig, E. Pervaiz, M. Azad, Z. Jahan, M. B. K. Niazi, and S. M. J. C. I. Baig, "NiFe2O4/SiO2 nanostructures as a potential electrode material for high rated supercapacitors," vol. 47, no. 9, pp. 12557-12566, 2021.

[13]   A. M. Navarro-Suárez *et al.*, "2D titanium carbide/reduced graphene oxide heterostructures for supercapacitor applications," vol. 1, no. 1, pp. 33-38, 2018.

[14]   Y. Gogotsi and R. M. J. A. n. Penner, "Energy storage in nanomaterials–capacitive, pseudocapacitive, or battery-like?," vol. 12, ed: ACS Publications, 2018, pp. 2081-2083.

[15]   M. S. Akhtar, I. H. Gul, M. M. Baig, M. A. J. M. S. Akram, and E. B, "Binder-free pseudocapacitive nickel cobalt sulfide/MWCNTs hybrid electrode directly grown on nickel foam for high rate supercapacitors," vol. 264, p. 114898, 2021.

[16]   M. Mumtaz, M. Hassan, S. Ullah, and Z. J. C. Ahmad, "Nanohybrids of multi-walled carbon nanotubes and cobalt ferrite nanoparticles: High performance anode material for lithium-ion batteries," vol. 171, pp. 179-187, 2021.

[17]   N. Bhalla *et al.*, "Doping independent work function and stable band gap of spinel ferrites with tunable plasmonic and magnetic properties," vol. 21, no. 22, pp. 9780-9788, 2021.

[18]   J. Sánchez-Martín *et al.*, "High-Pressure X-ray Diffraction and DFT Studies on Spinel FeV2O4," vol. 13, no. 1, p. 53, 2022.

[19]   W. Zhang *et al.*, "Structural and magnetic properties of Ni–Cu–Co ferrites prepared from sol-gel auto combustion method with different complexing agents," vol. 816, p. 152501, 2020.

[20]   J. J. E. Coey, "Perspective and prospects for rare earth permanent magnets," vol. 6, no. 2, pp. 119-131, 2020.

[21]   C. de Julian Fernandez, C. Sangregorio, J. de la Figuera, B. Belec, D. Makovec, and A. J. J. o. P. D. A. P. Quesada, "Progress and prospects of hard hexaferrites for permanent magnet applications," vol. 54, no. 15, p. 153001, 2021.

[22]   F. Sabry, *Holographie: Wie die Technologie funktioniert und Anwendungsfälle in der Industrie im wirklichen Leben*. One Billion Knowledgeable, 2022.

[23]   S. B. Narang, K. J. J. o. M. Pubby, and M. Materials, "Nickel spinel ferrites: a review," vol. 519, p. 167163, 2021.

[24]   L. N. Warr and G. H. Grathoff, "Geoscientific Applications of Particle Detection and Imaging Techniques with Special Focus on Monitoring Clay Mineral

Reactions," in *Handbook of Particle Detection and Imaging*: Springer, 2021, pp. 945-962.

[25]   S. C. Tolani, A. Golhar, and K. Rewatkar, "A review of morphological, structural behaviour and technological applications of ferrites," in *AIP Conference Proceedings*, 2019, vol. 2104, no. 1: AIP Publishing.

[26]   V. V. Jadhav, R. S. Mane, P. V. Shinde, V. V. Jadhav, R. S. Mane, and P. V. J. B.-F.-B. E. S. Shinde, "Basics of ferrites: structures and properties," pp. 37-45, 2020.

[27]   R. C. J. P. i. M. S. Pullar, "Hexagonal ferrites: A review of the synthesis, properties and applications of hexaferrite ceramics," vol. 57, no. 7, pp. 1191-1334, 2012.

[28]   P. Dhiman, R. Jasrotia, D. Goyal, and G. T. J. M. R. F. Mola, "Hexagonal ferrites, synthesis, properties and their applications," vol. 112, p. 336, 2021.

[29]   N. Kumari, S. Kour, G. Singh, and R. K. Sharma, "A brief review on synthesis, properties and applications of ferrites," in *AIP conference proceedings*, 2020, vol. 2220, no. 1: AIP Publishing.

[30]   S. B. Shelke, *Studies on the Structural, Electrical and Magnetic Properties of Some Substituted Spinel Ferrites*. Insta Publishing, 2020.

[31]   S. Kumar, P. Bhushan, S. J. E. Bhattacharya, chemical, and m. sensors, "Fabrication of nanostructures with bottom-up approach and their utility in diagnostics, therapeutics, and others," pp. 167-198, 2018.

[32]   V. Arole and S. J. J. M. S. Munde, "Fabrication of nanomaterials by top-down and bottom-up approaches-an overview," vol. 1, pp. 89-93, 2014.

[33]   S. Hamatani, D. Kitagawa, R. Maegawa, and S. J. M. A. Kobatake, "Photochromic behavior of diarylbenzene nanoparticles prepared by top-down and bottom-up approaches," vol. 3, no. 2, pp. 1280-1285, 2022.

[34]   P. Pattekari, Z. Zheng, X. Zhang, T. Levchenko, V. Torchilin, and Y. J. P. C. C. P. Lvov, "Top-down and bottom-up approaches in production of aqueous nanocolloids of low solubility drug paclitaxel," vol. 13, no. 19, pp. 9014-9019, 2011.

[35]   A. E. Danks, S. R. Hall, and Z. J. M. H. Schnepp, "The evolution of 'sol–gel'chemistry as a technique for materials synthesis," vol. 3, no. 2, pp. 91-112, 2016.

[36]   S. B. Somvanshi, M. V. Khedkar, P. B. Kharat, and K. J. C. I. Jadhav, "Influential diamagnetic magnesium (Mg2+) ion substitution in nano-spinel zinc ferrite

(ZnFe2O4): thermal, structural, spectral, optical and physisorption analysis," vol. 46, no. 7, pp. 8640-8650, 2020.

[37] M. E. Taygun and A. Boccaccini, "Nanoscaled bioactive glass particles and nanofibers," in *Bioactive Glasses*: Elsevier, 2018, pp. 235-283.

[38] G. Tartaro, H. Mateos, D. Schirone, R. Angelico, and G. J. N. Palazzo, "Microemulsion microstructure (s): A tutorial review," vol. 10, no. 9, p. 1657, 2020.

[39] T. Tatarchuk, M. Bououdina, J. Judith Vijaya, and L. John Kennedy, "Spinel ferrite nanoparticles: synthesis, crystal structure, properties, and perspective applications," in *Nanophysics, Nanomaterials, Interface Studies, and Applications: Selected Proceedings of the 4th International Conference Nanotechnology and Nanomaterials (NANO2016), August 24-27, 2016, Lviv, Ukraine*, 2017, pp. 305-325: Springer.

[40] O. F. Odio, E. J. M. s.-s. Reguera, properties, and applications, "Nanostructured spinel ferrites: Synthesis, functionalization, nanomagnetism and environmental applications," pp. 185-216, 2017.

[41] B. Liu *et al.*, "New Energy Storage Option: Toward ZnCo2O4 Nanorods/Nickel Foam Architectures for High-Performance Supercapacitors," *ACS Applied Materials & Interfaces,* vol. 5, no. 20, pp. 10011-10017, 2013/10/23 2013.

[42] L. T. Teixeira *et al.*, "Sustainable cellulose nanofibers-mediated synthesis of uniform spinel Zn-ferrites nanocorals for high performances in supercapacitors," vol. 24, no. 11, p. 9169, 2023.

[43] E. J. Alex and B. G. Manju, "Enhanced electrochemical properties of nanostructured Bi0. 9Gd0. 1FeO3 thin film as electrode material for super capacitors," 2023.

[44] A. Kumar *et al.*, "Transition-Metal-Substituted Nanoporous Manganese Ferrites Mn0. 95M0. 05Fe2O4 (M: Co, Cu, and Zn) as Electrode Materials for High-Performance Supercapacitors in Redox-Active Nonaqueous Electrolytes," vol. 37, no. 9, pp. 6810-6823, 2023.

[45] A. ur Rehman, Z. Batool, M. Ahmad, M. W. Iqbal, A. ul Haq, and H. J. J. o. E. C. Hegazy, "Impact of ZnO on structural and electrochemical properties of silver spinel ferrites for asymmetric supercapacitors," vol. 931, p. 117206, 2023.

[46] S. Manori, A. Manori, and R. K. Shukla, "Ferrite Nanoparticles for Energy Storage Applications," in *Engineered Ferrites and Their Applications*: Springer, 2023, pp. 189-197.

[47]   M. Mahmoud, A. M. Elshahawy, and T. J. J. o. E. S. Taha, "Lithium dopant assisted surface modification Zn ferrites for high-performance supercapacitor applications," vol. 68, p. 107881, 2023.

[48]   S. Jo, S. Pak, Y.-W. Lee, S. Cha, J. Hong, and J. I. J. I. J. o. E. R. Sohn, "Enhancing the electrochemical energy storage performance of bismuth ferrite supercapacitor electrodes via simply induced anion vacancies," vol. 2023, 2023.

[49]   A. E. Reddy, T. Anitha, C. V. M. Gopi, S. S. Rao, B. Naresh, and H.-J. J. A. m. Kim, "Construction of novel nanocomposite ZnO@ CoFe 2 O 4 microspheres grown on nickel foam for high performance electrochemical supercapacitors," vol. 10, no. 2, pp. 223-229, 2018.

[50]   M. B. Askari, P. Salarizadeh, M. Seifi, M. H. Ramezan zadeh, and A. Di Bartolomeo, "ZnFe2O4 nanorods on reduced graphene oxide as advanced supercapacitor electrodes," *Journal of Alloys and Compounds,* vol. 860, p. 158497, 2021/04/15/ 2021.

[51]   F. O. Agyemang and H. Kim, "Electrospun ZnFe2O4-based nanofiber composites with enhanced supercapacitive properties," *Materials Science and Engineering: B,* vol. 211, pp. 141-148, 2016/09/01/ 2016.

[52]   K. Karthikeyan, D. Kalpana, and N. G. Renganathan, "Synthesis and characterization of ZnCo2O4 nanomaterial for symmetric supercapacitor applications," *Ionics,* vol. 15, no. 1, pp. 107-110, 2009/02/01 2009.

[53]   Ravina *et al.*, "Synthesis and investigations of structural, surface morphology, electrochemical, and electrical properties of NiFe2O4 nanoparticles for usage in supercapacitors," vol. 34, no. 10, p. 868, 2023.

[54]   P. B. Kharat, S. B. Somvanshi, E. A. Dawi, A. M. Mopari, and N. H. J. J. o. M. S. M. i. E. Bansod, "Exploring the electrochemical performance of nickel-zinc ferrite nanoparticles for supercapacitor applications," vol. 35, no. 8, p. 606, 2024.

[55]   M. Saghafi and S. Zangeneh, "Zn-Co oxide electrodes with excellent capacitive behavior for using supercapacitor application," *Current Applied Physics,* vol. 19, no. 6, pp. 745-755, 2019/06/01/ 2019.

[56]   S. Pawar, S. Patil, M. Chithra, S. C. Sahoo, and P. Patil, "Cobalt ferrite nanoparticles for supercapacitor application," in *AIP Conference Proceedings*, 2020, vol. 2265, no. 1: AIP Publishing.

[57]   M. B. Askari and P. J. I. J. o. H. E. Salarizadeh, "Binary nickel ferrite oxide (NiFe2O4) nanoparticles coated on reduced graphene oxide as stable and high-performance asymmetric supercapacitor electrode material," vol. 45, no. 51, pp. 27482-27491, 2020.

[58]   C. Yang *et al.*, "Interfacial electrochemical investigation of 3D space-confined MnFe2O4 for high-performance ionic liquid-based supercapacitors," vol. 331, p. 135386, 2020.

[59]   D. Parajuli, S. Uppugalla, N. Murali, A. Ramakrishna, B. Suryanarayana, and K. Samatha, "Synthesis and characterization MXene-Ferrite nanocomposites and its application for dying and shielding," *Inorganic Chemistry Communications,* vol. 148, p. 110319, 2023/02/01/ 2023.

[60]   I. A. Alsafari, S. Munir, S. Zulfiqar, M. S. Saif, M. F. Warsi, and M. Shahid, "Synthesis, characterization, photocatalytic and antibacterial properties of copper Ferrite/MXene (CuFe2O4/Ti3C2) nanohybrids," *Ceramics International,* vol. 47, no. 20, pp. 28874-28883, 2021/10/15/ 2021.

[61]   Z. Jiang *et al.*, "3D Mesoporous Ni(OH)2/WS2 Nanofibers with Highly Enhanced Performances for Hybrid Supercapacitors," *Energy Technology,* vol. 7, no. 3, 2019.

[62]   G. Wang, L. Zhang, and J. J. C. S. R. Zhang, "A review of electrode materials for electrochemical supercapacitors," vol. 41, no. 2, pp. 797-828, 2012.

[63]   L. L. Zhang and X. J. C. s. r. Zhao, "Carbon-based materials as supercapacitor electrodes," vol. 38, no. 9, pp. 2520-2531, 2009.

[64]   Y. Xu, Z. Lin, X. Huang, Y. Liu, Y. Huang, and X. J. A. n. Duan, "Flexible solid-state supercapacitors based on three-dimensional graphene hydrogel films," vol. 7, no. 5, pp. 4042-4049, 2013.

[65]   Z. Ma *et al.*, "Layer-opened graphene paper with carbon nanotubes as support in a flexible electrode material for supercapacitors," vol. 775, pp. 982-989, 2019.

[66]   B. E. Conway, *Electrochemical supercapacitors: scientific fundamentals and technological applications*. Springer Science & Business Media, 2013.

[67]   L. Verger, C. Xu, V. Natu, H.-M. Cheng, W. Ren, and M. W. Barsoum, "Overview of the synthesis of MXenes and other ultrathin 2D transition metal carbides and nitrides," *Current Opinion in Solid State and Materials Science,* vol. 23, no. 3, pp. 149-163, 2019/06/01/ 2019.

[68]   D. Dhamodharan, M. A. Al-Harthi, B. Ramya, A. Bafaqeer, and F. Alam, "MXenes: A promising material with multifunctional applications," *Journal of Environmental Chemical Engineering,* vol. 12, no. 2, p. 112316, 2024/04/01/ 2024.

[69]   M. M. Baig, I. H. Gul, S. M. Baig, and F. Shahzad, "2D MXenes: Synthesis, properties, and electrochemical energy storage for supercapacitors – A review," *Journal of Electroanalytical Chemistry,* vol. 904, p. 115920, 2022/01/01/ 2022.

[70] D. Andhare, S. Jadhav, M. Khedkar, S. B. Somvanshi, S. More, and K. Jadhav, "Structural and chemical properties of ZnFe2O4 nanoparticles synthesised by chemical co-precipitation technique," in *Journal of Physics: Conference Series*, 2020, vol. 1644, no. 1, p. 012014: IOP Publishing.

[71] D. Ravinder, G. R. Mohan, and D. J. M. L. Sagar, "High frequency dielectric behaviour of aluminium-substituted lithium ferrites," vol. 44, no. 3-4, pp. 256-260, 2000.

[72] V. Shakeel, I. H. Gul, P. John, and A. J. S. P. J. Bhatti, "Biocompatible gelatin-coated ferrite nanoparticles: A magnetic approach to advanced drug delivery," vol. 32, no. 6, p. 102066, 2024.

[73] I. Gul, A. Maqsood, M. Naeem, M. N. J. J. o. a. Ashiq, and compounds, "Optical, magnetic and electrical investigation of cobalt ferrite nanoparticles synthesized by co-precipitation route," vol. 507, no. 1, pp. 201-206, 2010.

[74] A. A. Bunaciu, E. G. UdriŞTioiu, and H. Y. J. C. r. i. a. c. Aboul-Enein, "X-ray diffraction: instrumentation and applications," vol. 45, no. 4, pp. 289-299, 2015.

[75] Y. Zhu *et al.*, "Carbon-based supercapacitors produced by activation of graphene," vol. 332, no. 6037, pp. 1537-1541, 2011.